



저작자표시-비영리-동일조건변경허락 2.0 대한민국

이용자는 아래의 조건을 따르는 경우에 한하여 자유롭게

- 이 저작물을 복제, 배포, 전송, 전시, 공연 및 방송할 수 있습니다.
- 이차적 저작물을 작성할 수 있습니다.

다음과 같은 조건을 따라야 합니다:



저작자표시. 귀하는 원저작자를 표시하여야 합니다.



비영리. 귀하는 이 저작물을 영리 목적으로 이용할 수 없습니다.



동일조건변경허락. 귀하가 이 저작물을 개작, 변형 또는 가공했을 경우에는, 이 저작물과 동일한 이용허락조건하에서만 배포할 수 있습니다.

- 귀하는, 이 저작물의 재이용이나 배포의 경우, 이 저작물에 적용된 이용허락조건을 명확하게 나타내어야 합니다.
- 저작권자로부터 별도의 허가를 받으면 이러한 조건들은 적용되지 않습니다.

저작권법에 따른 이용자의 권리는 위의 내용에 의하여 영향을 받지 않습니다.

이것은 [이용허락규약\(Legal Code\)](#)을 이해하기 쉽게 요약한 것입니다.

[Disclaimer](#)

Thesis for the M. S. Degree

Atmospheric Correction Technique in SAR Interferometry for Monitoring Volcanic Activities

화산 활동 관측을 위한 SAR 간섭 기법에서의
대기 보정 기법

2013 년 2 월

서울대학교 대학원

지구환경과학부

정정교

Atmospheric Correction Technique in SAR Interferometry for Monitoring Volcanic Activities

화산 활동 관측을 위한 SAR 간섭 기법에서의
대기 보정 기법

지도 교수 김 덕 진

이 논문을 이학석사 학위논문으로 제출함
2013 년 2 월

서울대학교 대학원
지구환경과학부
정정교

정정교의 이학석사 학위논문을 인준함
2013 년 2 월

위 원 장 _____ 이 준 기 _____ (인)

부위원장 _____ 김 덕 진 _____ (인)

위 원 _____ 이 훈 열 _____ (인)

ABSTRACT

Ground deformation in volcano is a consequence of changes in magma chamber's volume. Magma storage, migration and volume change is closely associated phenomena with the ground deformation. Therefore, measuring ground deformation provides important information to understand the volcanic activities. For some specific volcanoes, such as Shinmoedake volcano, ground deformation of even a few centimeters can occur before eruption. Thus, measuring ground deformation needs to be fairly accurate.

SAR interferometry is a potential technique to measure the ground deformation accurately. One of the limitations in SAR interferometry, however, is atmospheric phase delay effects, which are induced when microwave propagates into the atmosphere. In this aspect, various methods for mitigating atmospheric phase delay effects have been developed. This study aims to mitigate the atmospheric phase delay especially in volcano because the stratified and turbulent atmospheric phase delay effects could severely contaminate the deformation patterns.

First method used in this study is the atmospheric correction technique using MODIS data. Multispectral observation can measure the integrated water vapor in the atmosphere by analyzing ratios of water vapor absorbing channel and atmospheric window channel. It can be

directly used for calculating the tropospheric phase delay effect caused by water vapor. Recent researches using multispectral datasets are restricted to approach using ENVISAT. Therefore, new approach is necessary in application using ALOS PALSAR. This study evaluates the applicability and possibility. In adequate temporal difference and cloud coverage, available datasets of MODIS successfully converted to the atmospheric phase delay corresponding to SAR acquisition time. However, there are some limitations in application into all dataset because of the cloud cover and temporal difference between the SAR acquisition time and MODIS acquisition time. In spite of limitations, the use of MODIS data in atmospheric correction yield better results and minimize misinterpreted errors.

The WRF model complements the limitations of MODIS data. In this respect, an application of the WRF model in atmospheric correction of differential interferogram was carried out in the second methods. The estimated APS from the WRF model can explain the stratified APS involved in differential interferograms. However, the accuracy of model prediction should be evaluated. The direct use of the WRF model predictions for atmospheric correction yield errors for mitigating the turbulent APS and the small-scaled APS.

Final approach is a time-series analysis. In model experiments, several properties of atmospheric phase screen (APS) are found out. The

first is that APS could remain in a time-series analysis and mainly comes from the stratified APS. The second is that it is possible to estimate and minimize the stratified APS by using sufficient WRF models. In the case of the turbulent APS, time-weighting low pass filtering is capable to reduce it. Therefore, the main idea of the atmosphere corrected time-series analysis adopt the stratified APS and turbulent APS correction method using WRF model and time-weighting methods. In comparison with observational dataset such as GPS and MODIS dataset, the estimated ground deformation and APS from the atmosphere corrected method have low rms errors, and high correlation. Therefore, this method can be believed as an accurate approach for measuring the ground deformation in volcanic region.

Keywords : SAR Interferometry, Atmospheric phase delay effect, Volcano

Students Number : 2011-20380

TABLES OF CONTENTS

ABSTRACT	3
TABLES OF CONTENTS	6
LIST OF FIGURES.....	8
LIST OF TABLES	14
1. INTRODUCTION	15
1.1. SAR INTERFEROMETRY AND VOLCANO MONITORING	15
1.2. ATMOSPHERIC PHASE DELAY IN INSAR	17
1.3. OBJECTIVES OF THIS RESEARCH.....	20
2. THE THEORETICAL BASIC OF SAR INTERFEROMETRY AND TIME-SERIES ANALYSIS.....	22
2.1. SAR INTERFEOMETRY	22
2.2. DIFFERENTIAL SAR INTERFEROMETRY	28
2.3. TIME-SERIES ANALYSIS	35
3. STUDY AREA AND DATASET	43
3.1. STUDY AREA.....	43
3.2. DATA	45
4. ATMOSPHERIC CORRECTION IN INDIVIDUAL DIFFERENTIAL INTERFEROGRAMS	50
4.1. DIFFERENTIAL SAR INTERFEROMETRY	50
4.2. ATMOSPHERIC PHASE DELAY EFFECTS SIMULATION	50

4.3.	RESULTS	63
5.	ATMOSPHERIC CORRECTION USING TIME-SERIES ANALYSIS .	70
5.1.	APS ESTIMATION ERRORS IN TIME-SERIES INSAR	71
5.2.	PROPERTIES OF APS IN TIME AND SPACE	76
5.3.	APPLICATION TO AVAILABLE DATASET AND DATA PROCESSING	88
5.4.	COMPARISON BETWEEN CONVENTIONAL AND ATMOSPHERE CORRECTED TIME SERIES ANALYSIS	95
5.5.	VALIDATION.....	101
6.	CONCLUSION	108
	REFERENCES.....	111

LIST OF FIGURES

Fig. 1. Geometry of interferometric SAR. The master and slave SAR images are marked with M and S. \mathbf{B}_{\perp} and \mathbf{B}_{\parallel} are perpendicular baseline and parallel baseline between two SAR satellites. \mathbf{R}_M and \mathbf{R}_S are the distance between the radar and the target in master and slave respectively. θ and θ_0 are incidence angle in respect to target on the topography and reference ellipsoid.	24
Fig. 2. Complex interferogram with perpendicular baseline of 11m between 2007-01-07 and 2007-11-25 in Shinmoedake volcano. This interferogram has the phase of the topographic contribution and ellipsoid.....	27
Fig. 3. Complex interferogram with perpendicular baseline of 11m. This interferogram has the phase of the topographic contribution after reference surface contribution was removed.	27.
Fig. 4. A schematic figure of differential interferogram in volcano activities monitoring. The repeat pass interferometry uses phase shift information between the master and slave SAR acquisition time. The phase difference is associated with the ground deformation induced by the volume change of magma chamber.	29
Fig. 5. Deformation error induced by DEM error. The deformation error is larger in differential interferogram as perpendicular baseline is long and DEM error is large.....	30

Fig. 6. A schematic figure of tropospheric classification using phenomenal characteristics in differential interferogram. (a) the turbulent atmospheric phase delay is uncorrelated with geometry (b) the stratified atmospheric phase delay is usually found at the mountain.	33
Fig. 7. Flow chart of Persistent Scatterer Interferometry (PSInSAR) and Small Baseline Subset algorithm (SBAS)	42
Fig. 8. Topographic map of Shinmoedake volcano. Yellow squares are the locations of the GPS stations. Red circle is the location of a radiosonde station.	44
Fig. 9. Differential Interferograms.....	51
Fig. 10. Conversion from precipitable water vapor to radar phase delay.	52
Fig. 11. Precipitable water vapor from MODIS data at 2007-11-25, 2008-04-11, 2008-05-27, 2011-03-05, and 2011-04-20	54
Fig. 12. Measured atmospheric phase delay from MODIS data	12
Fig. 13. Precipitable water vapor from WRF model.....	13
Fig. 14. Comparison of vertical profile between radiosonde and WRF model. Black lines mean the vertical profile of water vapor in a column measured by radiosonde. Red lines are the simulated vertical profiled from WRF mode.	58

Fig. 15. Time series of the integrated precipitable water vapor (IPWV). The IPWV derived from the radiosonde data have a good agreement with that from the WRF model predictions.	60
Fig. 16. Atmospheric correction using MODIS data. A.1. the uncorrected unwrapped differential interferogram from pair of 2008-05-27 and 2011-03-05 A.2. the atmospheric phase delay simulation using MODIS data A.3. the atmosphere corrected differential interferogram B.1. the uncorrected unwrapped differential interferogram from pair of 2008-05-27 and 2011-03-05 B.2. the atmospheric phase delay simulation using MODIS data. B.3. the atmosphere corrected differential interferogram.....	66
Fig. 17. Comparison of differential interferogram and simulated APS from MODIS generated from a pair of 2008-05-27-2011-04-20 across the red line in Fig.16	67.
Fig. 18. Comparison of differential interferograms and simulated atmospheric phase delay using WRF model. The selected differential interferograms have the 46 days interval. So, the ground deformation can be ignorable.	69
Fig. 19. Residual APS after processing SBAS.	74
Fig. 20. Residual APS after processing PSInSAR algorithm.....	75
Fig. 21. Stratified APS estimation method. The precipitable water vapor profiles	

measured by Radiosonde were integrated in column at each height. Blue line means the linear fitting with height and red line is the 2nd order fitting. ... 79

Fig. 22. Mean velocity (cm/yr) of simulated ground deformation. (a) Simulated ground deformation. (b) Simulated ground deformation and estimated turbulent APS (c) Simulated ground deformation and estimated stratified APS. In mean velocity map, turbulent APS seems to affect the ground deformation. However, it does not mean the variation of turbulent APS is large. In the same respect, the stratified APS can affect severely the ground deformation in time series analysis. 83

Fig. 23. Time series analysis with time window 720, 365, 243, 182, and 146 days for temporal low pass filtering. (a) The time series of the simulated ground deformation. (b) The time series of simulated ground deformation and estimated turbulent APS (c) Time series of simulated ground deformation and estimated stratified APS 84

Fig. 24. Time series plots of the sum of ground deformation and total APS (a), after atmospheric correction using stratified APS estimated from WRF model (b), after atmospheric correction using stratified APS estimated from simulated differential interferograms (c), residual of two approaches (d), (e). In every approach, low pass filtering method was applied with 730, 365 and 182days. 85

Fig. 25. Flow chart of atmosphere corrected PSInSAR.....	86
Fig. 26. Flow chart of atmosphere corrected SBAS	87
Fig. 27. (a) Differential interferogram from pair between 2008-05-27 and 2009-10-15 and (b) estimated stratified APS corresponding to the same date.....	93
Fig. 28. Scatter plot of unwrapped phase of Ifms and height between 2008-05-27 and 2009-10-15 (a) and 2008-05-27 and 2011-03-05 (b). Blue triangles are the phase in Shinmoedake volcano and gray crosses represent the phase in the region except Shinmoedake volcano. Red line is estimated APS from WRF model.....	94.
Fig. 29. A. ground deformation rate (cm/yr) in 2010 measured by conventional SBAS. B. simulated atmospheric phase delay effect rate(cm/yr) in 2010. C. Atmosphere corrected ground deformation rate (cm/yr) calculated by proposed method.	96
Fig. 30. Ground deformation measured from conventional PSInSAR (StaMPS). Maximum value of ground deformation is shown at 2009-08-30	99
Fig. 31. Ground deformation measured from atmosphere corrected PSInSAR (StaMPS).	100
Fig. 32. Comparison between ground deformations. Black line is LOS displacement measured from GPS (West GPS-East GPS). Blue triangles are the ground	

deformation estimated from conventional SBAS and red circles are the
 estimated from atmosphere corrected SBAS..... 104

Fig. 33. Comparison of ground deformations measured at location of west GPS (a)
 and east GPS(b). Blue line is LOS displacement measured by GPS. Green
 circles are the ground deformation estimated from conventional PSInSAR
 and red crosses are that estimated from atmosphere corrected PSInSAR 104

Fig. 34. (a) Stratified APS and (b) estimated turbulent APS from atmosphere corrected
 PSInSAR in 2011-04-20..... 105

Fig. 35. Estimated APS between 2008-05-27 and 2011-04-20. A. the simulated APS
 from MODIS data. B. the estimated APS from conventional PSInSAR C. the
 estimated APS from atmosphere corrected PSInSAR 106

Fig. 36. (a) The scatter plot between the estimated APS from MODIS and
 conventional PSInSAR between 2008-05-27 and 2011-04-20 (b) The scatter
 plot between the estimated APS from MODIS and atmosphere corrected
 PSInSAR 107

LIST OF TABLES

Table 1. Comparison of conventional DInSAR, PSInSAR, and SBAS	41
Table 2. ALOS PALSAR dataset used in this study from Jan. 2007 to Apr. 2011	47
Table 3. MOD05_L2 dataset used in this study.	48
Table 4. WRF setting parameters.....	49
Table 5. Correlation coefficient and RMS error between vertical profiles of the radiosonde and WRF model	61
Table 6. Available ALOS PALSAR pair for SBAS	90
Table 7. Available ALOS PALSAR dataset for PSInSAR.	92

1. Introduction

1.1. SAR Interferometry and volcano monitoring

Synthetic Aperture Radar (SAR) records the complex digital numbers of reflected signal from distributed targets. The amplitude of SAR image reflects the slope distribution, dielectric constant, and roughness of targets. The SAR amplitude information can be used in geological mapping and classification of targets. SAR Interferometry (InSAR) utilizes phase information of SAR images. Phase information is closely related to the distance between targets and radar. SAR interferometry (InSAR) has been known as a powerful technique to measure the ground movement and generate the digital elevation map. Space-borne and air-borne SAR interferometry can provide high resolution topographic information in extensive areas. [Q. Lin et al., 1994; B. Rabus et al., 2003, M. Crosetto, 2002; A. Reigber and A. Moreira, 2000]. Differential interferometry (DInSAR) can detect small change of topography as well. Recently, DInSAR technique is widely applied into numerous phenomena which accompany the ground movement such as earthquake, urban subsidence, and land slide [M. Simons et al., 2002; X. Ye et al., 2004; M. Tesauero et al., 2000]. The DInSAR technique can detect the ground deformation up to a fraction of the microwave wavelength. Thus, the accuracy of DInSAR can

theoretically reach a few centimeters in line of sight. However, its performances are limited due to surface decorrelations. If targets on the surface change rapidly or the surface condition is modified, InSAR technique cannot provide any information due to the decorrelations. In spite of these limitations, utilization of various approaches such as polarimetric SAR interferometry, tandem mission, and multiple baseline implementation can overcome the weakness of InSAR. Therefore, InSAR and DInSAR technique have potential to explain the Earth and Environmental phenomena.

Volcanic activities often cause the massive casualties, economic losses and environmental damages. To alleviate the damages, predicting when and where volcanoes will erupt should be resolved. Volcanic eruption mechanism is correlated with the migration, accumulation and stress triggering of magma. For monitoring and detecting these phenomena, numerous methods have been applied such as seismic wave observation, infrasound monitoring, and ground deformation measurement [F. Brenguier et al., 2008; J.B. Johnson et al., 2004; J.B. Shepherd et al., 1998].

Numerous researches have identified and measured the ground deformation caused by volcanic activities [Z. Lu et al., 2010; G. Wadge et al., 2006]. To understand volcanic activities, it requires the spatially extensive information. Although dense GPS stations could be a good

measurement system, difficulties of installation and maintenance of GPS station can be limited in active volcanoes. One of the advantages of SAR interferometry is that it can complement these limitations. Additionally, the SAR interferometry can measure volcanic movement in line of sight (LOS) with a few centimeters accuracy and in an extensive area. The investigation of volcanism using DInSAR technique reveals the magma chamber system and migration of magma, volcanic inflation and deflation and so on [S. Jonsson et al., 1999; P.A. Rosen et al., 1996; S. Yun et al., 2006]. Therefore, SAR interferometry has been evaluated as a powerful method to measure the volcanic phenomena.

1.2. Atmospheric phase delay in InSAR

InSAR measurement usually contains several diverse error factors such as phase noise, baseline errors, DEM errors, and atmospheric phase delay [R. Hassen et al., 1999]. Therefore, careful interpretation is necessary in interpreting interferogram. The atmospheric phase delays are generated when microwave propagates into the atmosphere, which could seriously contaminate differential interferograms. Atmospheric phase delays can have 10-14 cm errors in deformation measurement by a 20% spatial or temporal change in relative humidity [H.A. Zebker et al., 1997]. Thus, atmospheric effect should be taken into account for monitoring of

accurate deformations. The mitigation of atmospheric phase delay in InSAR and DInSAR is one of the issues to be solved for generating the DEM and measurement of ground deformation.

In order to minimize atmospheric phase delay, many researches exploited and developed atmospheric correction techniques. These atmospheric correction techniques can be categorized into several groups. The first group uses the phase information in SAR images and geometric data. The isolation of atmospheric effect from deformation is easy where deformation occurs far from a summit of volcano because the stratified atmospheric phase delay effects correlate with its height [F. Beauducel et al., 2000]. However, in the case that major deformation is observed around a summit, an extraction of deformation is more difficult because atmospheric effects are likely to be correlated with deformation in time.

The second group corrects the differential interferograms using auxiliary dataset such as multi-spectral and meteorological data. [Z. Li et al., 2005] proposed a method for correcting atmospheric effects using Medium Resolution Imaging Spectrometer (MERIS) data and Moderate-Resolution Imaging Spectroradiometer (MODIS), which are onboard ENVISAT. Thus, the acquisition time of ASAR is coincident to that of MERIS. It means that the retrieved water vapor from MERIS can represent the microwave propagation delay. As a result, this technique was able to mitigate the atmospheric phase delay effect in DInSAR. The main

advantage in this approach is the MERIS data are independent to SAR images. It represents that the atmospheric phase delay effect involved in individual Differential Interferograms can be corrected. The limitation of this method is the lack of multi-spectral data to retrieve the water vapor in the atmosphere. The water vapor retrieval algorithm of MERIS is sensitive to the presence of cloud. The cloudy area is impossible to estimate the water vapor information and only a few differential interferogram could be mitigated. Additionally, atmospheric correction method using MERIS is applicable only to ASAR differential interferograms due to different acquisition time of satellites. Another approach for atmospheric correction is the method using weather forecasting model such as MM5 or WRF [J. Foster et al., 2006; G.Nico et al., 2011]. Meso-scale weather forecasting model calculate and re-simulate the atmospheric condition based on the re-analysis data. Depending on the accuracy of model and input data, the reliability of the calculated atmospheric conditions is determined. It is possible to simulate the water vapor contents, pressure and temperature etc. regardless of cloud presence. Even though the model results relevant to the cloud cover might be inaccurate, the influence on the atmospheric phase delay is applicable [H.A. Zebker et al., 1997]. However, model results should be estimated for atmospheric correction because of accuracy of their results. Numerous researches can yield successful results using WRF model.

In contrast to above methods, without external data for atmospheric correction, statistical methods such as Permanent Scatterers SAR Interferometry (PSInSAR) and Small Baseline Subset algorithm(SBAS) exploit the main properties of deformation, DEM errors, noise and atmospheric phase delay effect [A. Ferretti et al., 2000; P. Berardino et al., 2002]. The main idea to isolate the atmospheric phase delay effect from ground deformation is that the atmospheric phase delay effect is usually randomly generated while the ground deformation is correlated in time. Thus, the uncorrelated atmospheric phase delay effects are possibly mitigated by spectral filtering. However this assumption is not always valid because the seasonality of atmospheric condition could be left. In this case, residual of the atmospheric phase delay effect can be interpreted as deformation.

1.3. Objectives of this research

In this research, the atmospheric correction techniques will be evaluated in the individual differential interferogram generated by ALOS PALSAR data using multispectral data. Until now, only ENVISAT ASAR Interferograms were corrected using MERIS and MODIS data. This technique is applicable to only ENVISAT ASAR differential interferogram. Thus, for atmospheric correction in ALOS PALSAR differential

interferogram, new approach is necessary. Thus, atmospheric correction technique will be proposed and evaluated.

Secondly, the atmospheric correction technique using meso-scale weather forecasting model will be applied. In this research, Weather Research and Forecasting model (WRF) is the next generation model after MM5. This research aims to simulate the atmospheric phase delay using WRF model and evaluate its capability in volcanic area.

Thirdly, the properties of the atmospheric phase delay in time series analysis of differential interferograms will be investigated. The multi-temporal atmospheric phase delay simulation using WRF model can explain how much the atmospheric phase delay contaminates the ground deformation resulted from time-series analysis and might propose new approach to mitigate more realistic atmospheric phase delay.

Finally, the ground deformation in volcano region will be measured using atmosphere corrected time-series analysis. Through a methodological comparison between conventional time-series analysis and atmosphere corrected time-series analysis, ignored errors in conventional time-series analysis will be reconsidered and corrected.

2. The theoretical basic of SAR interferometry and time-series analysis

2.1. SAR Interfeometry

2.1.1. Brief description about SAR Interferometry

SAR Interferometry utilizes the phase information of two satellite images which observe the same area from slightly different angles. The microwave transmitted from the radar reaches scatterers on the ground and comes back to the radar. The phase difference of each target introduces different delay. This implies that phase information is related to the distance between targets and radar. However, the signal of phase is periodic and should be expressed by the integer multiple of the wavelength. It means that the recorded phase in SAR images is a last fraction of the two-way distance and always smaller than the microwave wavelength. This can be achieved at same time or different time by repeated orbits of the same satellite. The former is the case the radar sensor is mounted on the same platform and the latter is usually performed in general satellites such as ERS-1,-2, ENVISAT, ALOS, TerraSAR-X, etc. For the latter case, time intervals are various depending on the platform.

The repeat pass SAR interferometry is suitable for space-borne SAR

system since the installation is restricted in satellite platform. Because technically the satellite cannot be at the same position, the baseline between acquisition positions is induced. These different look angles of different positions generate the topographic information.

2.1.2. *Geometric configuration of InSAR*

Fig. 1 demonstrates the geometry of InSAR. The M and S is the master and the slave position, respectively. If there is only one dominant scatterer in each resolution cell, the complex values of SAR images can be decomposed into amplitude and phase using

$$y_M = |y_M| \exp(j\phi_M) \quad y_S = |y_S| \exp(j\phi_S) \quad (1)$$

where y_M and y_S are the master and slave complex images, respectively. ϕ_M and ϕ_S are the phase of master and slave images.

After resampling the slave SAR image corresponding to the same location in the master SAR image, complex conjugate multiplication yields the complex interferograms.

$$y_M y_S^* = |y_M| |y_S| \exp(j(\phi_M - \phi_S)) \quad (2)$$

The actual phase values involve the distance information and scatterer's phase contribution.

$$\phi_M = -\frac{2\pi 2R_M}{\lambda} + \phi_{M.scat}$$

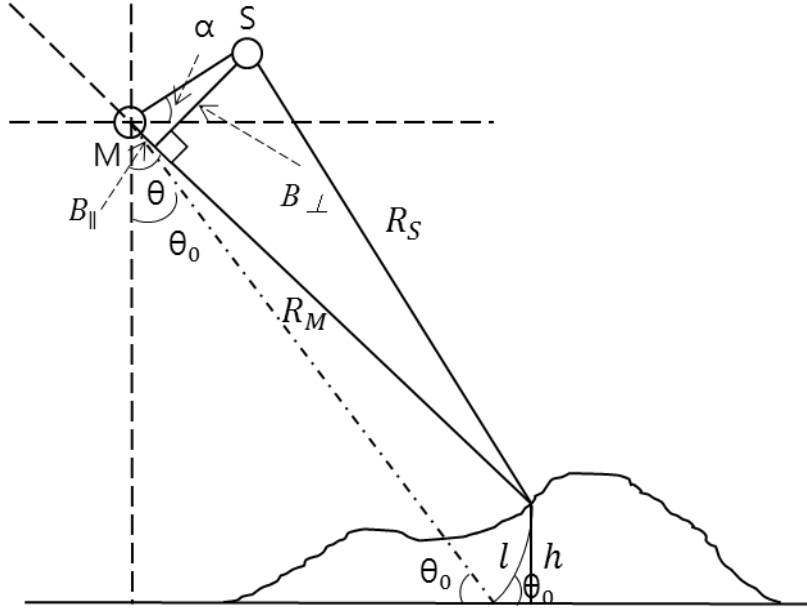


Fig. 1. Geometry of Interferometric SAR. The master and slave SAR images are marked with M and S. B_{\perp} and B_{\parallel} are perpendicular baseline and parallel baseline between two SAR satellites. R_M and R_S are the distance between the radar and the target in master and slave respectively. θ and θ_0 are incidence angle in respect to target on the topography and reference ellipsoid.

$$\phi_s = -\frac{2\pi 2R_s}{\lambda} + \phi_{s.scats} \quad (3)$$

where R is the distance between the radar and scatterers on the ground and ϕ_{scats} is the scatterer's phase contribution. If the conditions of the targets do not change, the characteristics of each scatterer can be assumed as equal.

$$\phi_{M.scats} = \phi_{s.scats} \quad (4)$$

So, the phase term of eq.2 can be rearranged into

$$\phi_M - \phi_s = -\frac{4\pi(R_M - R_s)}{\lambda} = -\frac{4\pi\Delta R}{\lambda} \quad (5)$$

If the ray of microwave is parallel, geometrically speaking, ΔR can be approximated as the following equation.

$$\Delta R = B\sin(\theta - \alpha) \quad (6)$$

$$\phi = -\frac{4\pi B\sin(\theta - \alpha)}{\lambda} \quad (7)$$

where ϕ is interferometric phase, B is baseline between master and slave position, θ is the look angle. This equation contains the phase contribution of topography and reference surface.

2.1.3. Phase contribution of topography and reference ellipsoid

Interferometric phase can be decomposed into the topographic contribution and reference surface contribution using physical phase observation and geometric configuration. The phase contribution of reference ellipsoid can be expressed as the following equation.

$$\phi_0 = -\frac{4\pi}{\lambda} B \sin(\theta_0 - \alpha) \quad (8)$$

where B is the baseline and θ_0 is the incidence angle in respect to the reference ellipsoid. The relation of incidence angles in respect to the reference surface and topography yields $\delta\theta = \theta - \theta_0$. Eq.8 explains only phase contribution of reference ellipsoid. The extraction of topography phase can be obtained by subtracting the reference phase contribution from the observed phase. For the sake of simplicity of calculation, eq.7 can be rearranged as follows.

$$\phi = -\frac{4\pi}{\lambda} B \sin(\theta_0 + \delta\theta - \alpha) \quad (9)$$

As a result, topographic phase contribution is found by combining eq.8 and eq.9.

$$\begin{aligned} \phi_{flat} = \phi - \phi_0 &= -\frac{4\pi}{\lambda} B [\sin(\theta_0 + \delta\theta - \alpha) - \sin(\theta_0 - \alpha)] \\ &= -\frac{4\pi}{\lambda} B \cos(\theta_0 - \alpha) \delta\theta = -\frac{4\pi}{\lambda} \frac{B_{\perp 0} h}{r \sin \theta_0} \end{aligned} \quad (10)$$

This equation expresses the topographic phase contribution in which InSAR is proportional to the perpendicular baseline. Thus, interferograms generated from pairs with long perpendicular baseline have more fringe patterns in topography than that with short perpendicular baseline. Technically, the above procedure is called “flattening”.

By inserting 2π into ϕ_{flat} , the sensitivity of topographic phase contribution (height ambiguity) can be achieved. It represents the height difference corresponding to a 2π phase shift.

$$h_a = -\frac{\lambda}{2\pi} \frac{r \sin \theta_0}{B_{\perp 0}} \quad (11)$$

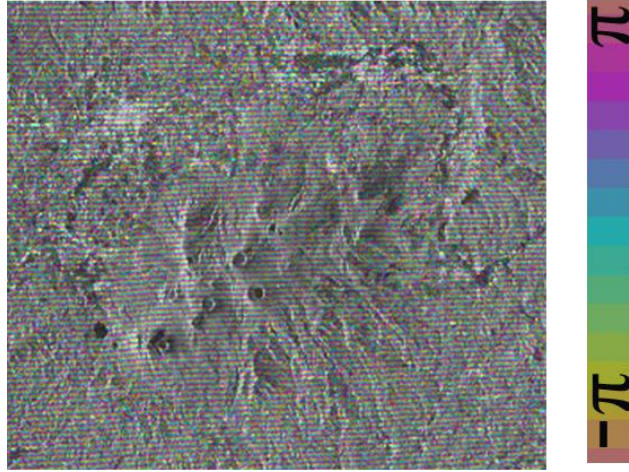


Fig. 2. The complex interferogram with perpendicular baseline of 11m between 2007-01-07 and 2007-11-25 in Shinmoedake volcano. This interferogram has the phase of the topographic contribution and ellipsoid.

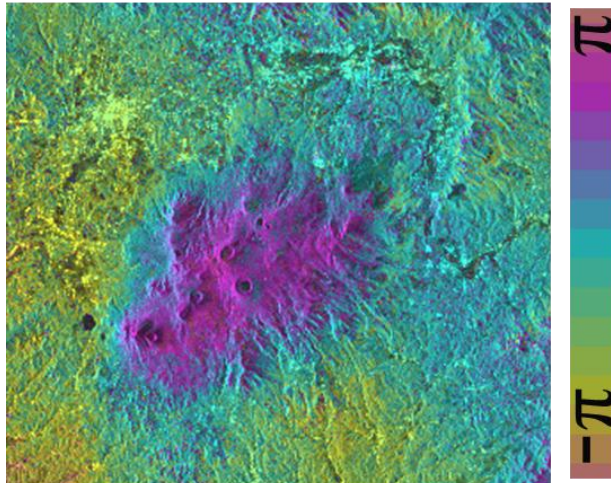


Fig. 3. The complex interferogram with perpendicular baseline of 11m. This interferogram has the phase of the topographic contribution after reference surface contribution was removed.

In general application for generation of DEM, the long perpendicular baseline is preferred because the number of the induced fringes from interferograms with long baseline is more than from the interferograms with short perpendicular baseline, if the unwrapping errors are ignorable.

2.2. Differential SAR Interferometry

2.2.1. *Deformation measurement*

Differential SAR Interferometry (DInSAR) aims to measure ground deformation. If ground deformation occurred in the region of interest, eq.7 can be rearranged as following:

$$\phi = -\frac{4\pi}{\lambda} \{ B \sin(\theta - \alpha) + d \} \quad (12)$$

For measuring ground deformation, topographic phase contribution needs to be simulated with the knowledge of its topography. There are several approaches to generate a differential interferogram. The first is that a topographic contribution removal is performed with an external elevation model such as SRTM and GTOPO [Massonnet et al., 1993]. The second method is the three-pass DInSAR [Zebker et al., 1994]. Topographic contribution is generated using the interferogram generated from the topographic pair with ignorable ground deformation. This topographic pair has to have sufficient coherence and sensitivity of height. In the case of the

three pass DInSAR, baseline should be scaled before subtracting the topographic pair from the deformation pair. The third method is the four-pass DInSAR. Basic concept of this method is the same as the three-pass DInSAR. The topographic pair with no expected ground deformation and the deformation pair with distinct ground deformation need to be selected based on the information of time span and coherence.

Basically, phase contributions involved in differential interferogram can be explained by

$$\phi_{diff} = \phi_{defo} + \phi_{DEM\ error} + \phi_{orbit\ error} + \phi_{APS} + \phi_{noise} \quad (13)$$

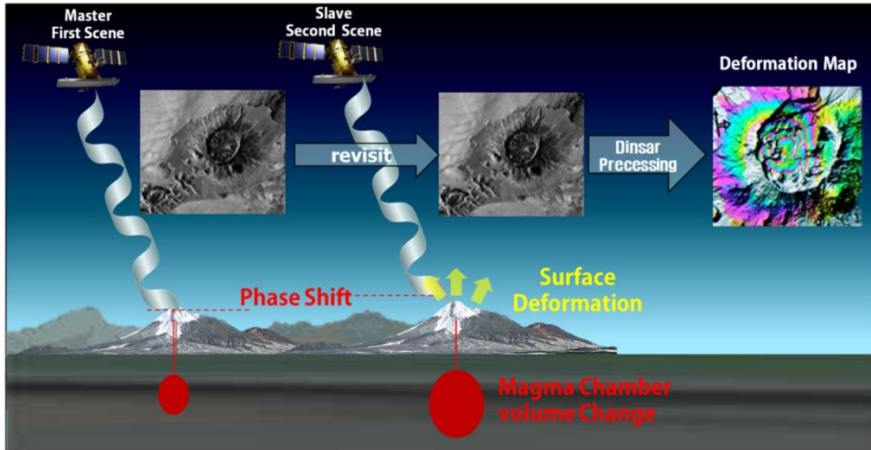


Fig. 4. A schematic figure of differential interferogram in volcano activities monitoring. The repeat pass interferometry uses phase shift information between the master and slave SAR acquisition time. The phase difference is associated with the ground deformation induced by the volume change of magma chamber.

where ϕ_{defo} is ground deformation, $\phi_{DEM\ error}$ is topographic error, ϕ_{APS} is atmospheric phase delay effect, $\phi_{orbit\ error}$ is orbital estimation error, and ϕ_{noise} is noise error.

Generally speaking, the deformation contribution in differential interferogram is more sensitive than the topographic error contribution. Both contributions in differential interferograms can be expressed as following.

$$\phi_{DEM\ error} = -\frac{4\pi}{\lambda} \frac{B_{\perp 0} h_{err}}{r \sin \theta_0} \quad (14)$$

$$\phi_{defo} = -\frac{4\pi}{\lambda} d \quad (15)$$

Under the assumption that the topographic error is below 10m, $\phi_{DEM\ error} \ll \phi_{defo}$ because r is much larger than $B_{\perp 0}$. Therefore, differential interferometry is valid to measure ground deformation and DEM error can be minimized with short perpendicular baseline.

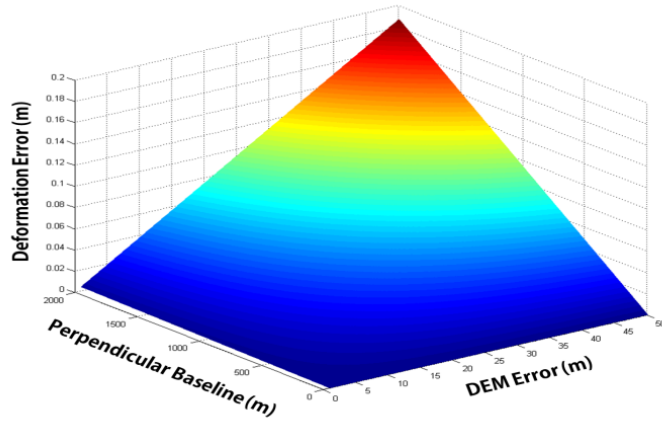


Fig. 5. The deformation error induced by DEM error. The deformation error is larger in differential interferogram as perpendicular baseline is long and DEM error is large.

2.2.2. *Atmospheric phase delay*

The atmospheric phase delay of microwave is the main limitation in the measurement of ground deformation using differential interferogram. The refractivity of microwave in air can be written as [E. K.Smith, and S. Weintraub ,1953].

$$\Delta L_d = \frac{1}{10^6 \cos \theta_{inc}} \int_0^H \left\{ k_1 \frac{P}{T} + \left(k'_2 \frac{e}{T} + k_3 \frac{e}{T^2} \right) - 4.03 \times 10^7 \frac{n_e}{f^2} + 1.4W \right\} \quad (16)$$

where ΔL_d is the total atmospheric delay, θ_{inc} is the incidence angle of incoming ray. P , T and e is air pressure in hPa, air temperature in Kelvin and partial water vapor pressure of the atmospheric column in hPa, respectively. n_e is electronic number density per cubic meter, f is the radar frequency. W represents the liquid water contents in g/m^3 . The constant values $k_1 = 77.6K \text{ hPa}^{-1}$, $k'_2 = 23.3K \text{ hPa}^{-1}$ and $k_3 = 3.75 \times 10^5 \text{ K}^2 \text{ hPa}^{-1}$ are used [E.K.Smith, and S.Weintraub, 1953]. Above equation explains different components which induce the atmospheric phase delay effects. The first component represents hydrostatic term which depends on dry parameters of the atmosphere such as temperature and air pressure. The second component means wet delay, atmospheric phase delay due to precipitable water vapour. The third component is phase delay in ionosphere. The third component represents liquid delay induced by atmospheric liquid water content. The tropospheric phase delay i.e. wet delay, hydrostatic delay and liquid water delay is independent of the

frequency while the ionospheric delay is a function of the frequency of microwave.

The precipitable water vapour is the main parameter of wet delay terms. The precipitable water vapour can be defined as

$$PWV = \frac{1}{\rho_l} \int \rho_v dh \quad (17)$$

where ρ_l is the density of liquid water (10^3 kg/m^3), and ρ_v is the density of water vapour.

The wet delay term in eq.16 can be expressed by

$$e = \rho_v R_v T \quad (18)$$

$$\Delta L_{wet.d} = \frac{1}{10^6 \cos \theta_{inc}} \rho_v R_v \left(k'_2 + k_3 \frac{1}{T_M} \right) PWV \quad (19)$$

where $R_v = 461.524 \text{ J/K kg}$ and T_M is weighted temperature of the column.

This equation denotes that left part of the wet delay term could be regarded as a typical constant [Bevis et al., 1994].

$$\Pi^{-1} = \frac{1}{10^6} \rho_l R_v \left(k'_2 + k_3 \frac{1}{T_M} \right) \approx 6.5 \quad (20)$$

Therefore, the wet delay term can be simplified as

$$\Delta L_{wet.d} = \frac{6.5 PWV}{\cos \theta_{inc}} \quad (21)$$

Ionospheric delay can be approximated by

$$\Delta L_{iono.d} = \frac{1}{10^6 \cos \theta_{inc}} \frac{K}{f^2} TEC \quad (22)$$

$$TEC = \frac{n_e}{f^2} \quad (23)$$

where $\Delta L_{iono.d}$ is ionospheric delay in meters, f is the frequency of the microwave and TEC is total electron content. The K is $-40.28 \text{ m}^3/\text{s}^2$ [Jakowski et al., 1992]. The ionospheric delay in L-band of ALOS

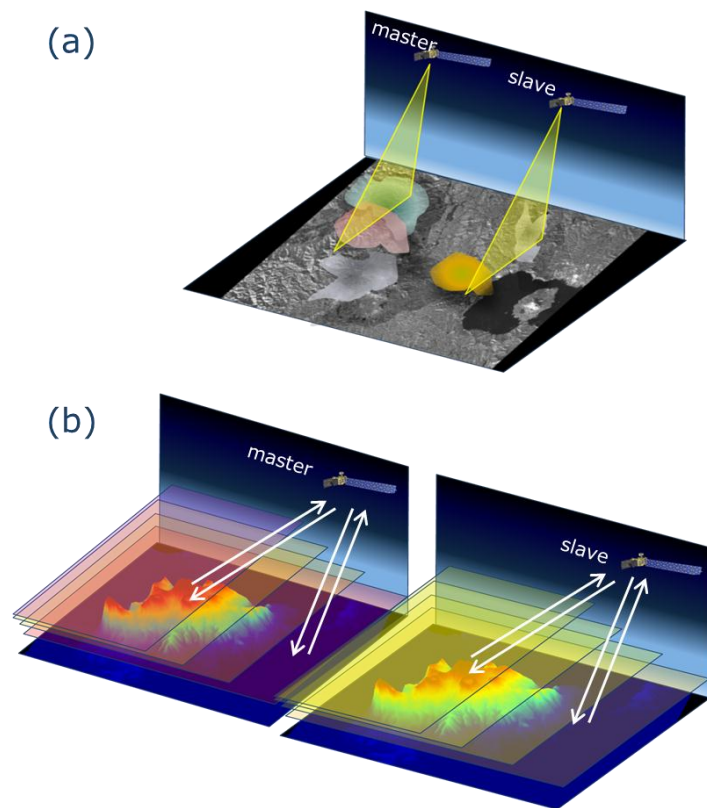


Fig. 6. A schematic figure of tropospheric classification using phenomenal characteristics in differential interferogram. (a) the turbulent atmospheric phase delay is uncorrelated with geometry (b) the stratified atmospheric phase delay is usually found at the mountain.

PALSAR yields approximately -2.4974×10^{-17} TEC. However, in differential interferogram, identical TEC at the same local time is canceled. Therefore, this effect normally can be ignorable [Hassen et al, 1999].

In most cases, the wet delay term is the most important source of errors in differential interferogram rather than other terms. The liquid water delay and hydrostatic delay reach only sub-millimeters and a few millimeters. Therefore, the accuracy of the atmospheric delay dominantly depends on the knowledge of the qualified precipitable water vapor.

Another approach to decompose the atmospheric phase delay uses phenomenal characteristics. Tropospheric effects can be classified into two groups in InSAR; one is the phase delay caused by turbulence and the other is different stratified troposphere [Hassen et al, 1999]. Turbulent atmospheric phase delay is independent to geometry while atmospheric phase delay effects caused by stratified troposphere usually appear as a function of height. Therefore, turbulent atmospheric phase delay randomly occurs in space. In the case of stratified atmospheric phase delay, different vertical refractivity induces the localized atmospheric phase delay especially in the mountain (Fig.6).

2.2.3. *Coherence and decorrelation*

The coherence γ between two SAR images is defined as

$$\gamma = \frac{|E\{y_1 y_2^*\}|}{\sqrt{E\{|y_1|^2\}E\{|y_2|^2\}}} \quad 0 \leq \gamma \leq 1 \quad (24)$$

where E is the ensemble average operator and y_1 and y_2 are the complex value of SAR images. The coherence can be used as a measure of quality of interferometric phase in each pixel. The change of the surface characteristics is the main cause of the loss of coherence. By using this property of coherence, the change detections and classification of scatterers were performed in applications into earth sciences [J.G.Liu et al., 2001; J.G.Liu et al., 2004; J. Askne and J.O. Hagberg, 1993].

Several factors causing the decorrelation can be distinguished into 1) baseline and geometric decorrelation (γ_{geom}) induced by slightly different incidence angle, 2) Doppler centroid decorrelation (γ_{dop}), 3) volume decorrelation (γ_{vol}) caused by multiple scattering signal, 4) thermal noise decorrelation ($\gamma_{thermal}$), 5) temporal decorrelation (γ_{temp}) caused by change of characteristic of scatterers and 6) processing decorrelation (γ_{proce}). The total decorrelation possibly involved in interferograms can be expressed by the following equation [Zebker and Villasenor, 1992]:

$$\gamma_{total} = \gamma_{geom} \times \gamma_{dop} \times \gamma_{vol} \times \gamma_{thermal} \times \gamma_{temp} \times \gamma_{proce} \quad (25)$$

2.3. Time-series analysis

In traditional differential interferograms, long time ground

deformation is hardly measured due to temporal decorrelation. Time-series analysis aims to overcome the limitations of traditional differential interferograms and estimate ground deformation accurately. Additionally, time-series analysis utilizes multi-baseline and multi-temporal differential interferograms in order to estimate the diverse errors such as DEM error, orbital error, random APS, and noise. The widely used time series analysis approaches are Persistent Scatterer Interferometry (PSInSAR) and Small Baseline Subset algorithms (SBAS) [A. Ferretti et al., 2000; P. Berardino et al., 2002].

2.3.1. Persistent Scatterer Interferometry

PSInSAR uses persistent scatterers which are less affected by temporal decorrelation and exhibit stable coherence over a long time interval, such as the artificial structures. The most important procedure in PSInSAR is the selection of persistent scatterers (PS). A general PS selection method can be carried out with the dispersion index (**Da**) [A. Ferretti et al., 2001]. **Da** can be defined as

$$D_a = \frac{\sigma_A}{m_A} \quad (26)$$

where m_A and σ_A are the mean and standard deviation of the amplitude value of complex SAR images. The numerical experiment about **Da** shows that the phase can be stable in low **Da** values and PS candidates are

selected under a threshold (typically $\mathbf{Da} < 0.25$).

However, this approach might be limited for human-made structures since most PS candidates are located in urban regions. To complement this limitation, other considerations were added into the PS selection method. Stanford Method for Persistent Scatterers (StaMPS) algorithm focuses on natural targets of which phase value are stable in time with low SNR (high \mathbf{Da}). For exploitation of these scatterers, StaMPS suggested the additional procedure i.e., phase stability analysis and phase noise computation with the relatively high \mathbf{Da} . (typically $\mathbf{Da} < 0.4$) [A. Hooper, 2006]. Another approach for PS selection of natural targets were suggested in SqueeSAR. SqueeSAR algorithm find distributed targets using DespeckKS algorithm [A. Ferretti et al., 2011].

2.3.2. *Small Baseline Subset*

The main idea of SBAS is the generation of differential interferograms which have small perpendicular baseline and linking separated differential interferograms. SBAS uses the properties that geometrical decorrelation can be minimized in differential interferograms when the difference of the incidence angles is extremely small.

The linking method is possible by generating the design matrix $\mathbf{A} [M \times N]$ where M is the number of differential interferograms and N is

the number of unknown factors i.e. phase values except at reference time.

Thus, differential interferograms set can be expressed as

$$A\phi = \delta\phi \quad (28)$$

where ϕ is the phase value at SAR acquisition time, $\delta\phi$ is a differential interferograms set. For example, if $\delta\phi_1 = \phi_3 - \phi_2$, $\delta\phi_2 = \phi_4 - \phi_1$, and $\delta\phi_3 = \phi_3 - \phi_0$, A would have the following form:

$$A = \begin{bmatrix} 0 & -1 & +1 & 0 \\ -1 & 0 & 0 & +1 \\ 0 & 0 & +1 & 0 \\ \dots & \dots & \dots & \dots \end{bmatrix} \quad (29)$$

To solve eq. 28, the rank of matrix is the remaining problem in making an inverse matrix of A. The singular value decomposition can decompose A matrix into

$$A = USV^T \quad (32)$$

,and its pseudo inverse matrix is

$$A^+ = VS^+U^T \quad (33)$$

To connect the phase value at separated time and avoid discontinuity in cumulative deformation, deformation should be converted to velocity and time parameters.

$$v^T = \left[v_1 = \frac{\phi_1}{t_1 - t_0}, \dots, v_N = \frac{\phi_N}{t_N - t_{N-1}} \right] \quad (34)$$

The eq.28 can be rewritten as

$$Bv = \delta\phi \quad (35)$$

If deformation model in time is valid, the model parameter p can be inserted eq 35.

$$v = Mp \quad (36)$$

$$B Mp = \delta \phi \quad (37)$$

2.3.3. *Processing algorithm*

After selecting PSs in PSInSAR and unwrapping of small baseline subset in SBAS, interferometric phases are exploited using the properties of several contributions. (eq.13) Even though the processing step might be different, the basic idea is similar.

- Basic concept to estimate residual of topographic contribution (DEM error) is proportional to the perpendicular baseline.

$$\phi_{DEM\ error} = -\frac{4\pi}{\lambda} \frac{B_{\perp 0} h_{err}}{r \sin \theta_0} \quad (38)$$

- Orbital error can be expressed by

$$\phi_{orbit\ error} = a l^T + p_{\xi} \xi^T + p_{\eta} \eta^T \quad (39)$$

where $a[K \times 1]$ is a constant phase value, $p_{\xi} [K \times 1]$ and $p_{\eta} [K \times 1]$ is linear phase components along the azimuth $\xi [H \times 1]$ and range $\eta [H \times 1]$, respectively, induced by the APS and orbital errors $B [K \times 1]$.

- Deformation is written by

$$\phi_{defo} = T v^T \quad (40)$$

where T is time vector and v is velocity matrix.

- The isolation of APS from deformation can be done using the assumption that APS is not correlated while deformation has correlation in

time. Thus, low pass operator in time is one of the methods for estimation of APS.

Table. 1. Comparison of conventional DInSAR, PSInSAR, and SBAS

	Conventional DInSAR	PSInSAR	SBAS
Atmospheric error	No reduction	Temporally uncorrelated APS reduction	Temporally uncorrelated APS reduction
Perpendicular baseline	Shorter is better	No limitation below critical baseline	Shorter is better
Master	Depending on interferogram	One master	Depending on interferogram
Pixel selection method	coherence	Dispersion index and additional approaches	coherence

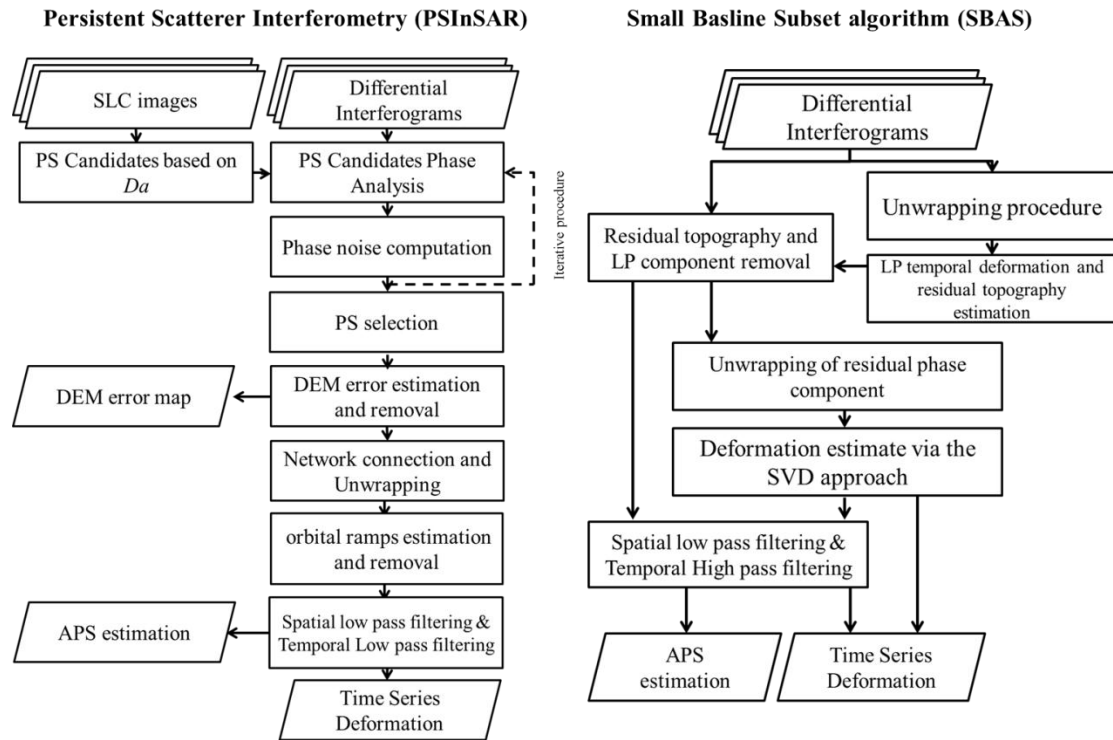


Fig. 7. Flow chart of Persistent Scatterer Interferometry (PSInSAR) and Small Baseline Subset algorithm (SBAS)

3. Study area and dataset

3.1. Study area

Mt. Shinmoedake, located in Kagoshima prefecture in Kyushu, Japan, is a part of the Kirishima cluster of volcanoes (Fig 8). Small scaled volcanic activities in Mt. Shinmoedake have been continued consistently. In 2008 and 2011, relatively large eruptions were observed. There is no eruption of magma in 2008, and only white smoke was detected while the accumulation of lava in its crater and massive volcanic ash were observed in 2011. According to the report of Japan Meteorological Agency (JMA), ground deformation in Shinmoedake volcano was not observed in 2008, and reached 3~4 cm in 2010 [霧島山の火山活動解説資料, 2011]. Thus, the atmospheric effect in this region seems to be of the same scale to the possible inflation of volcano caused by volume changes. Therefore, reducing the atmospheric effect is vital to measure ground deformation accurately.

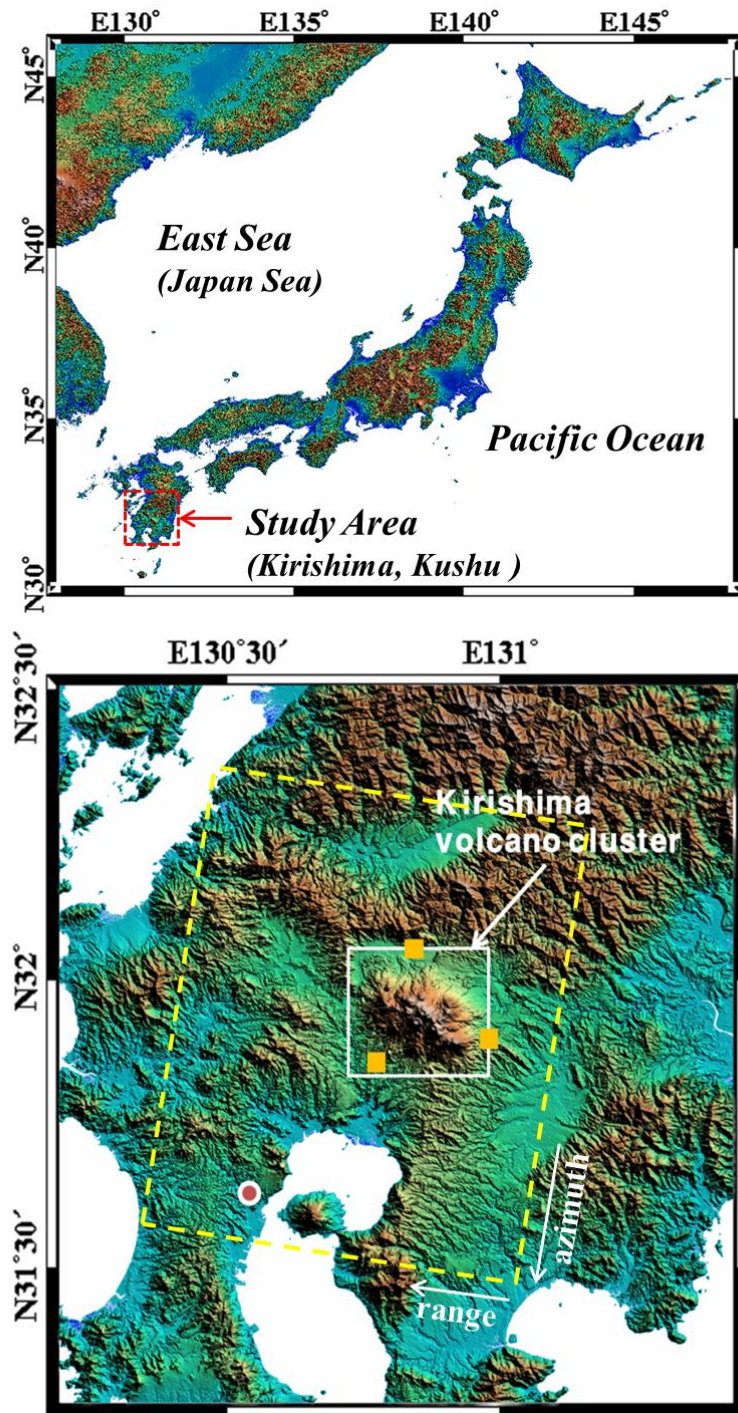


Fig. 8. Topographic map of Shinmoedake volcano. Yellow squares are the locations of the GPS stations. Red circle is the location of a radiosonde station.

3.2. Data

3.2.1. SAR data

19 ALOS PALSAR FBS data and 2 ALOS PALSAR FBD data were acquired in descending orbits over Shinmoedake around 1:45 UTC. ALOS scene covers approximately 75 km x 85 km from Jan 2007 to Apr 2011 (Table 2). L-band (1.27GHz) ALOS PALSAR data are relatively unaffected by temporal decorrelation. Thus, these data are appropriate to generate differential interferograms.

3.2.2. MODIS data

The Moderate Resolution Imaging Spectroradiometer (MODIS) installed on Terra and Aqua of NASA is an effective way to monitor the water vapor distribution in the troposphere. The retrieval algorithm for total precipitable water product (PWV) relies on observations of water vapor attenuation of near-infrared solar radiation (0.905, 0.936, and 0.94) reflected by Earth's surfaces [Y. J. Kaufman, et al., 1992]. The total precipitable water vapor products are provided in MOD05_L2 (TERRA) and MYD05_L2 (AQUA) with which the level 2 data are generated at the spatial resolution of 1 km. Although the resolution of the water vapor

product is relatively lower than that of ALOS, it can be used in the correction technique because the atmospheric effect extends over several kilometres. In this research, the MODIS data acquired within an hour of each of ALOS data were used.

3.2.3. *WRF model data*

The weather forecasting and research model (WRF model) is developed by National Center for Atmospheric Research (NCAR), Mesoscale and Microscale Meteorology Division and the National Centers for Environmental Prediction (NCEP), National Oceanic and Atmospheric Administration (NOAA). The WRF model is able to implement various meteorological parameters such as pressure, water mixing ratio, temperature, liquid water mixing ratio. In this study, the Advanced Research Weather and Forecasting Model, version 3.4, was setup. The NCEP final analysis (FNL) data were used as initial and time-dependent boundary condition data. The two way nested domains procedure were carried out at 27-, 9-, 3-, 1-km horizontal resolution. Among these domains, the 1 x 1 km resolution data were used in calculation of atmospheric delay. The top of the atmosphere of this setting model is 50 hPa and a total of 31 vertical levels were processed. Starting 6hr prior to the SAR acquisition time, 12-h simulations were conducted.

Table 2 ALOS PALSAR dataset used in this study from Jan. 2007 to Apr. 2011

Number	DATE(UTC)	TIME (UTC time)
1	2007-01-07	1:46 AM
2	2007-11-25	1:45 AM
3	2008-01-10	1:45 AM
4	2008-02-25	1:44 AM
5	2008-04-11	1:43 AM
6	2008-05-27	1:42 AM
7	2008-07-12	1:42 AM
8	2008-11-27	1:45 AM
9	2009-01-12	1:45 AM
10	2009-04-14	1:46 AM
11	2009-05-30	1:47 AM
12	2009-08-30	1:47 AM
13	2009-10-15	1:47 AM
14	2009-11-30	1:47 AM
15	2010-01-15	1:47 AM
16	2010-03-02	1:47 AM
17	2010-12-03	1:44 AM
18	2011-01-18	1:43 AM
19	2011-03-05	1:42 AM
20	2011-04-20	1:41 AM

Table 3. The MOD05_L2 dataset used in this study.

Number	DATE(UTC)	TIME (UTC time)	Cloud cover
1	2007-01-07	2:50 AM	Partly Cloudy
2	2007-11-25	2:40 AM	Cloud free
3	2008-01-10	2:50 AM	Cloudy
4	2008-02-25	1:25 AM	Cloudy
5	2008-04-11	1:40 AM	Cloud free
6	2008-05-27	1:50 AM	Cloud free
7	2008-07-12	2:05 AM	Cloudy
8	2008-11-27	2:40 AM	Cloudy
9	2009-01-12	1:45 AM	Cloudy
10	2009-04-14	1:40 AM	Cloudy
11	2009-05-30	1:50 AM	Cloudy
12	2009-08-30	2:15 AM	Cloudy
13	2009-10-15	2:25 AM	Cloudy
14	2009-11-30	2:40 AM	Cloudy
15	2010-01-15	2:50 AM	Cloudy
16	2010-03-02	1:25 AM	Cloudy
17	2010-12-03	2:40 AM	Cloudy
18	2011-01-18	2:50 AM	Cloudy
19	2011-03-05	1:25 AM	Cloud free
20	2011-04-20	1:40 AM	Cloud free

Table 4. WRF setting parameters.

WRF Model	In This Study
Reanalysis data	FNL data (6h data)
Spatial Resolution of WRF simulation	27km, 9km, 3km, <u>1 km</u>
Land Use	MODIS Land Use
DEM	SRTM DEM (90m)

4. Atmospheric Correction in Individual Differential Interferograms

4.1. Differential SAR Interferometry

The raw SAR data were focused to single look complex images. For the estimation of the baseline of each pair, the orbital location and FFT method were used [K. Zhang et al., 2009]. Interferogram dataset were selected based on the perpendicular and temporal baseline of each pair. After removing the phase effects of the topography and ellipsoid, adaptive Goldstein filtering were applied. The masking criteria were chosen based on the coherence maps. In several differential interferograms, the decorrelated areas were masked out. Unwrapping procedure was processed using the minimum cost flow algorithm [M. Costantini, 1998]. (Fig. 9)

4.2. Atmospheric Phase Delay Effects Simulation

4.2.1. Atmospheric Phase Delay Simulation using MODIS Data

In order to simulate atmospheric phase delay effect from MODIS data, available dataset should be identified. The MOD05_L2 and

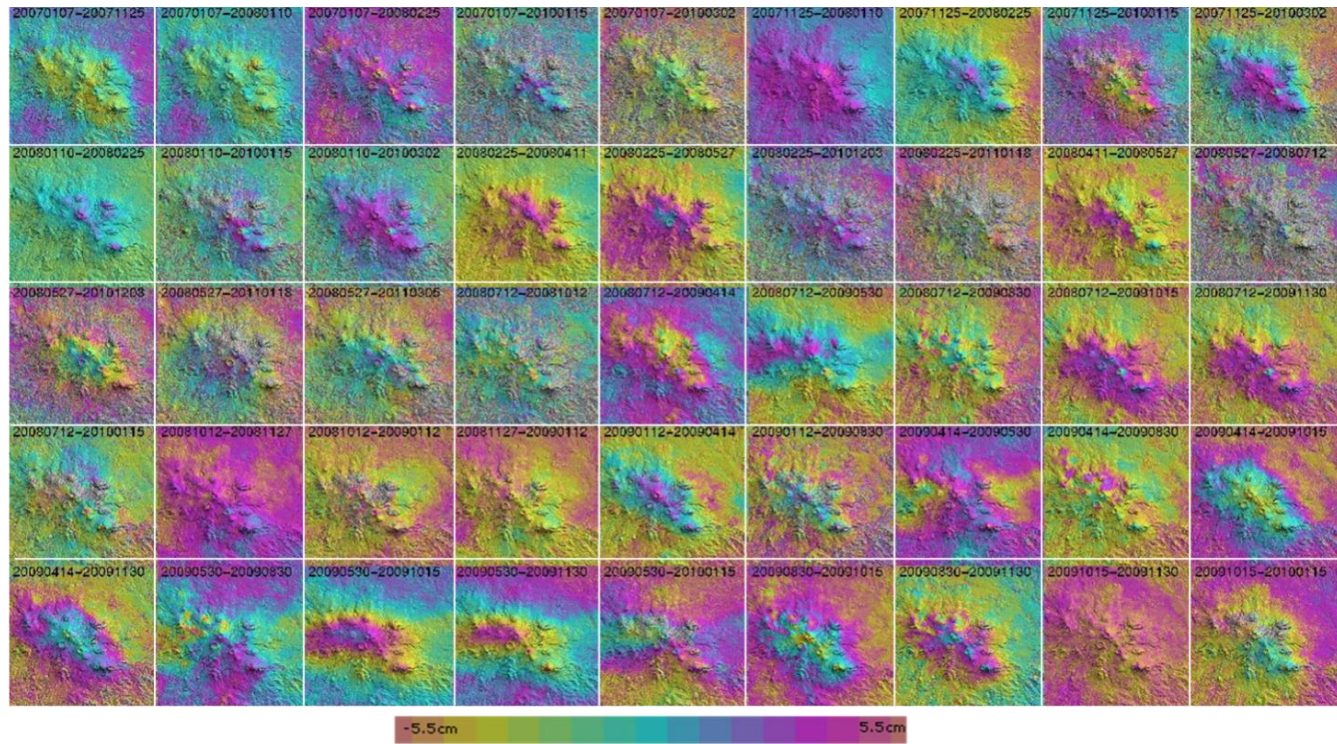


Fig. 9. Differential Interferograms

MYD05_L2 offer the information about precipitable water vapor (PWV) in the atmosphere. Precipitable water vapor is the dominant component to microwave delay. Thus, PWV data was converted to atmospheric phase delay effects. Fig. 10 describes the procedures to convert to atmosphere phase delay effects. First of all, the region of interest should be selected based on the coordinate of each pixel. The MOD05_L2 and MYD05_L2 have their own latitude and longitude coordinate information, however, the number of pixels is different from the PWV information. The PWV data have 2030 x 1354 pixels while the number of the geometric coordinates involved in MOD05 and MYD05 is 406 x 270. MOD03 and MYD03 provide geometric information in 1 km x 1km spatial resolution (2030 x 1354). More accurate geocoding procedure is possible if only using

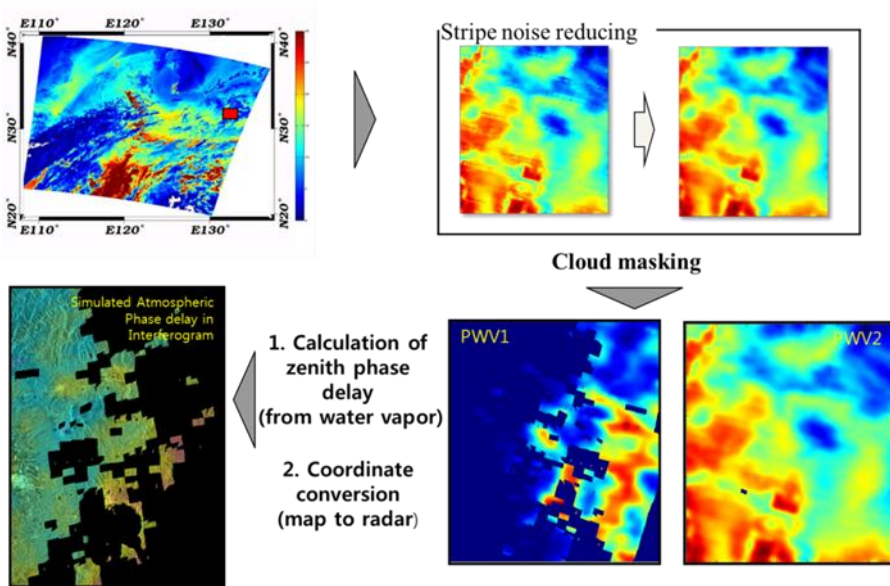


Fig. 10. Conversion from precipitable water vapor to radar phase delay.

MOD03 and MYD03. The next step is removing the stripe-shaped noise of MODIS. The stripe-shaped noise is induced by the radiometric calibration error. Since ALOS PALSAR covers broad areas, small noise may affect significant phase shift in interferograms. Until now, several techniques were suggested for removing the stripe noise in data, such as histogram matching, Fourier transform, and moment matching. In this study, Fourier transform method was used for removing noise because the stripe noises are periodic and have certain frequencies that are identifiable. After this procedure, whether the selected data are reliable or not should be determined. When clouds are present, data tend to overestimate the amount of water vapor and this error yields uncorrelated fringes with real atmospheric effects in DInSAR. Thus, the cloud area should be masked out using cloud mask data. Under cloud free condition, PWV images need to be coregistrated to SAR scenes. PWV data contain only water vapor amount, thus, conversion procedure is necessary (Fig. 10). Precipitable water vapor can be inverted to zenith path delay [Z. Li et al., 2005]. Corresponding equations can be described as follows,

$$\Pi^{-1} = \frac{ZWD}{PWV} = 10^{-6} \cdot \rho_w \cdot (k_2 + \frac{k'_3}{T_M}) \cdot \frac{R_0}{M_w} \quad (41)$$

$$\Pi^{-1} = 0.10200 + \frac{1708.08}{T_M} \quad (42)$$

where ZWD is zenith water vapor delay, PWV is precipitable water vapor, Π is conversion factor, ρ_w is water density, T_M represents weighted mean temperature in the troposphere and k_2' k_3' are the refractivity constant.

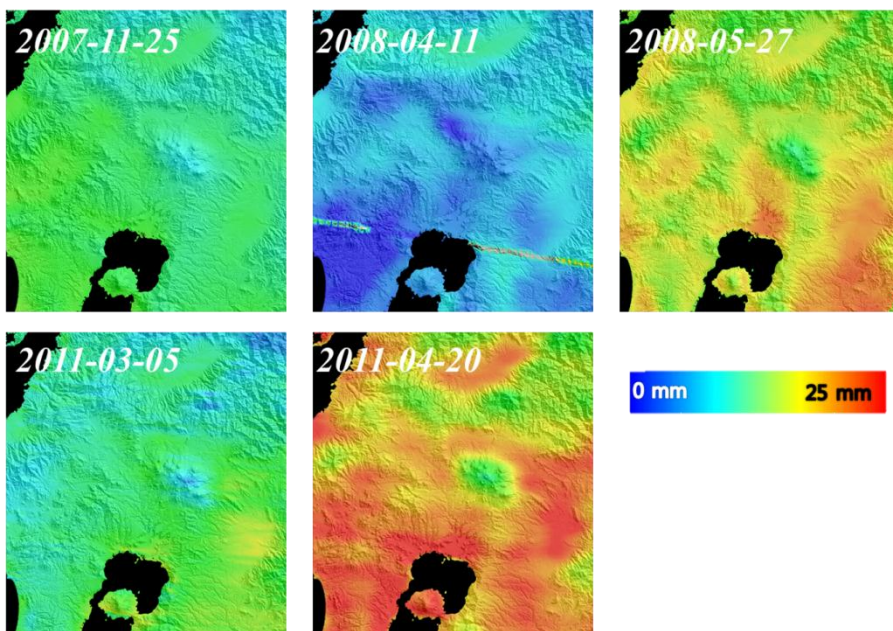


Fig. 11. Precipitable water vapor from MODIS data at 2007-11-25, 2008-04-11, 2008-05-27, 2011-03-05, and 2011-04-20

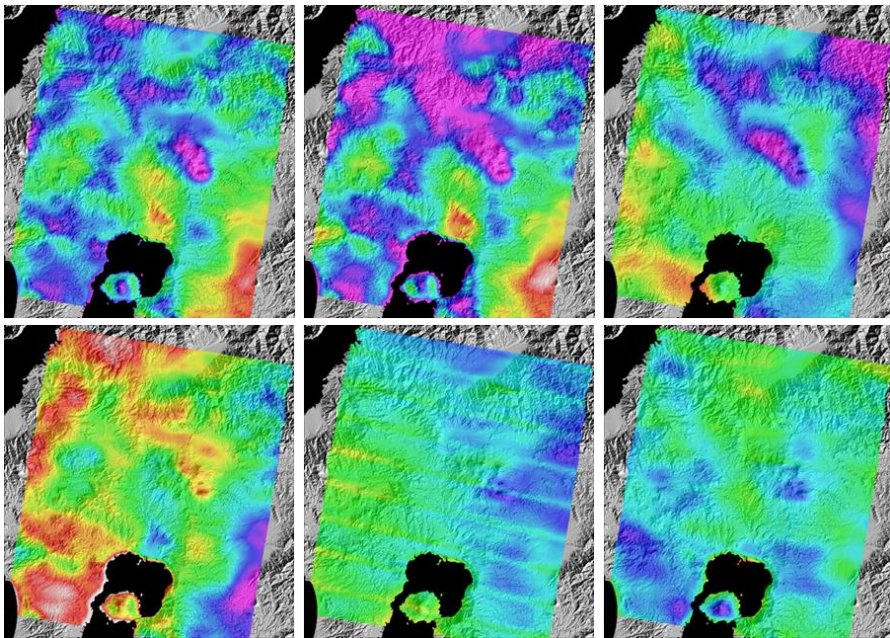


Fig. 12. Estimated atmospheric phase delay from MODIS data

It is possible to calculate how much atmospheric water vapor affects in differential interferograms using the difference between two ZWDs corresponding to SAR images (Fig. 12).

4.2.2. *Atmospheric Phase Delay Simulation using WRF Model*

The WRF model is able to implement pressure, water mixing ratio, temperature, liquid water mixing ratio and so on at 27-, 9-, 3-, and 1-km horizontal grid resolutions at desired time. Simulation procedures of the meteorological conditions were carried out at 1-km grids. These meteorological parameters resulted from the WRF model can be directly used in a simulation of wet delay and hydrostatic delay in atmospheric phase delay effects by using

$$e = \frac{QP}{0.622+Q} \quad (43)$$

$$\Delta L_d = \frac{1}{10^6 \cos \theta_{inc}} \int_0^H \left\{ k_1 \frac{P}{T} + \left(k'_2 \frac{e}{T} + k_3 \frac{e}{T^2} \right) \right\} \quad (44)$$

where Q is water vapor mixing ratio (g/kg), ΔL_d is the total atmospheric delay, θ_{inc} is the incidence angle of ray. P , T and e is air pressure in hPa, air temperature in Kelvin and partial water vapor pressure of the atmospheric column in hPa, respectively. The constant values of $k_1 = 77.6$, $k'_2 = 23.3$, $k_3 = 3.75 \times 10^5$ are used [Askne and H.Nordius, 1987]. Above equation explains the different components which induce atmospheric phase delay effects. The first component represents the hydrostatic term which depends on the dry parameters of the

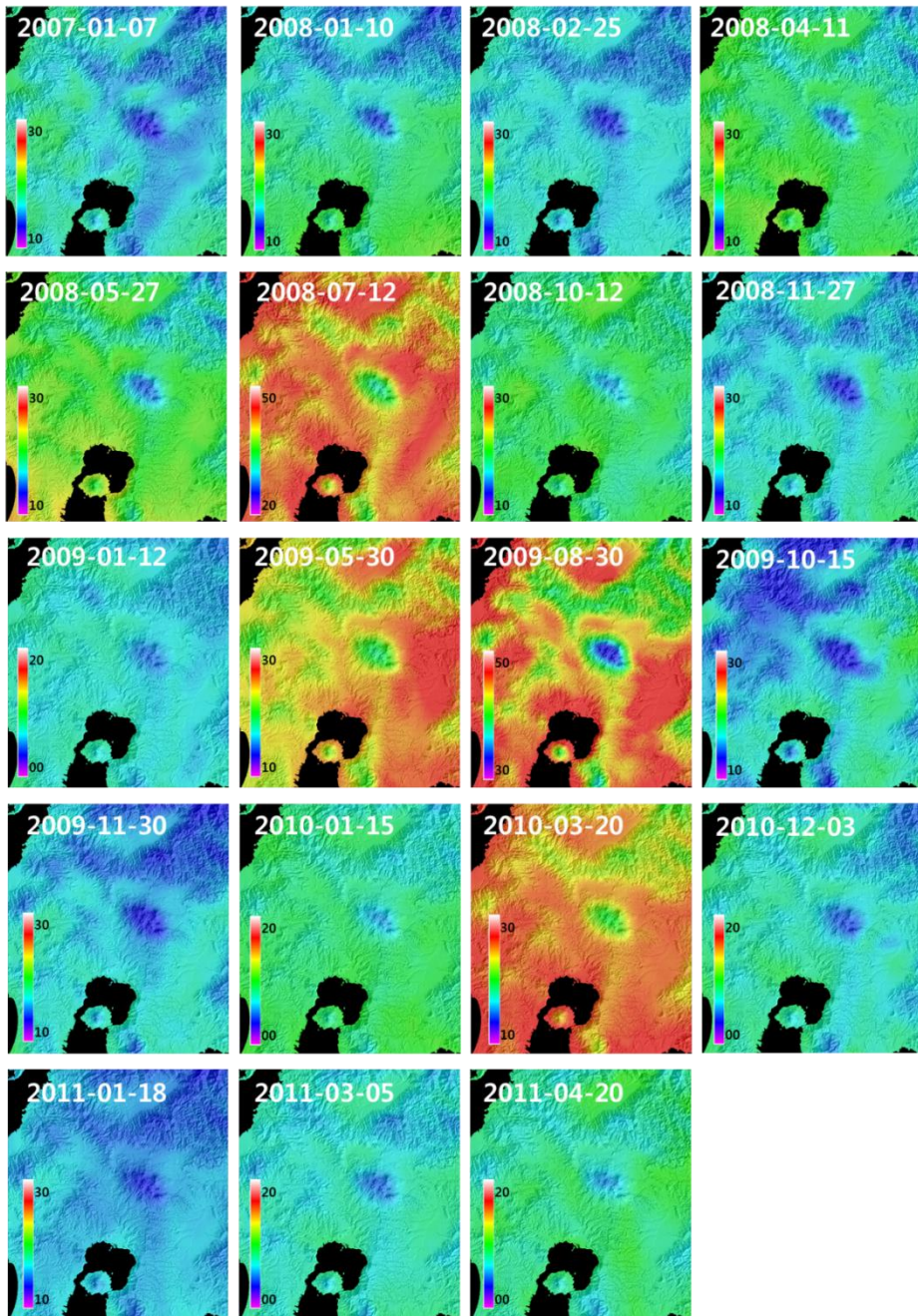


Fig. 13. Precipitable water vapor from WRF model.

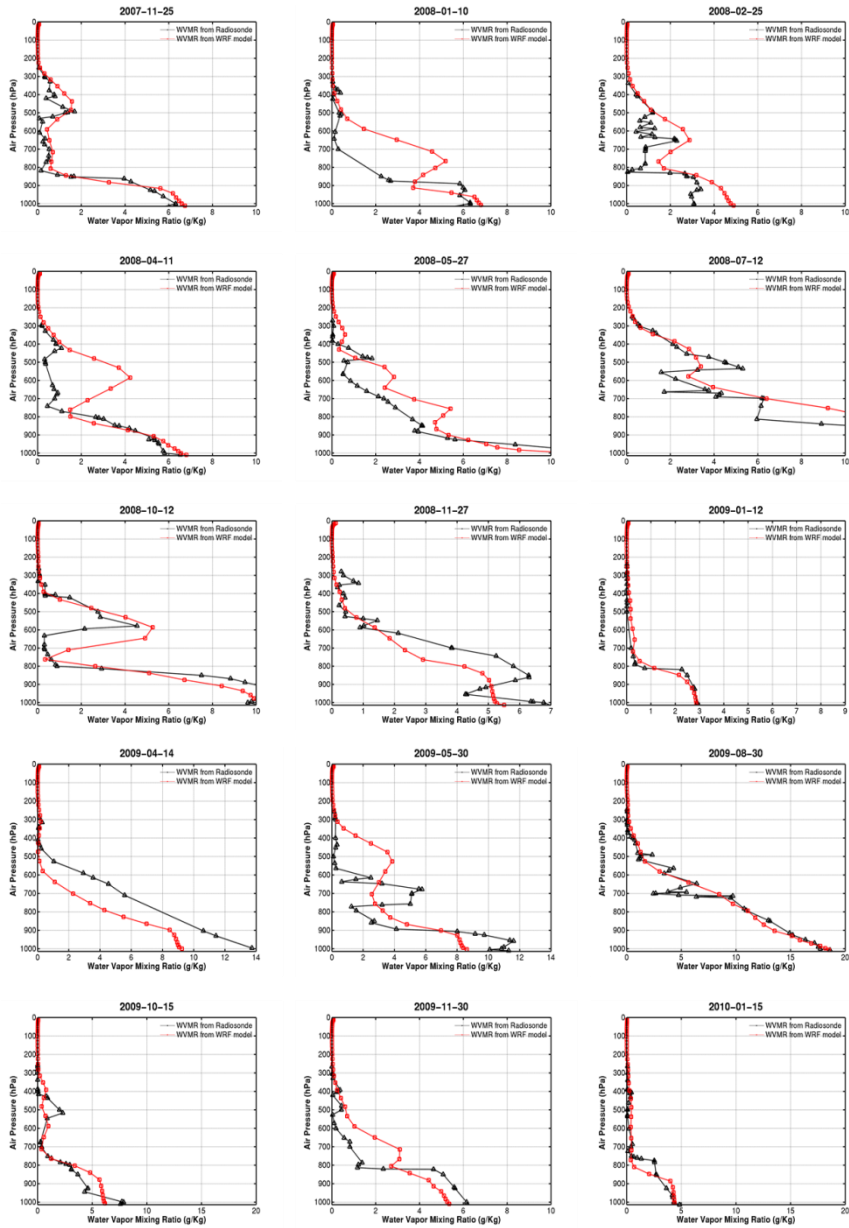


Fig. 14. Comparison of vertical profile between radiosonde and WRF model. Black lines mean the vertical profile of water vapor in a column measured by radiosonde. Red lines are the simulated vertical profile from WRF mode.

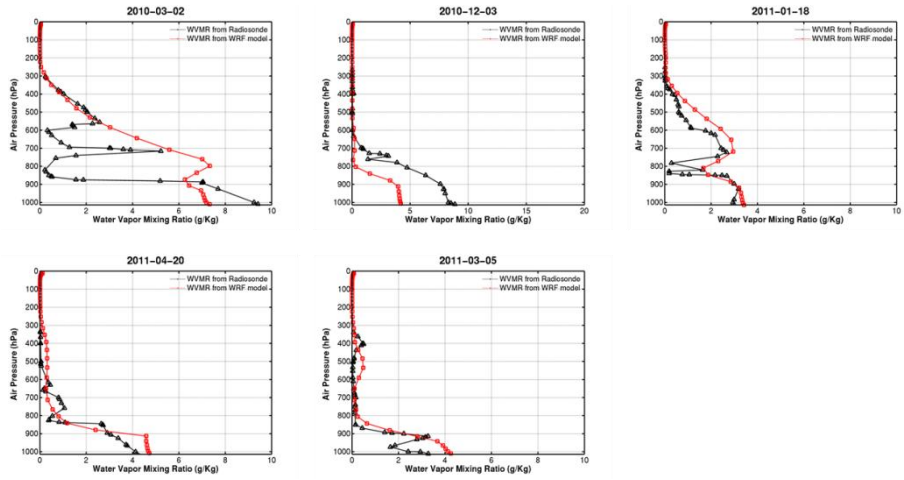


Fig.14. continued

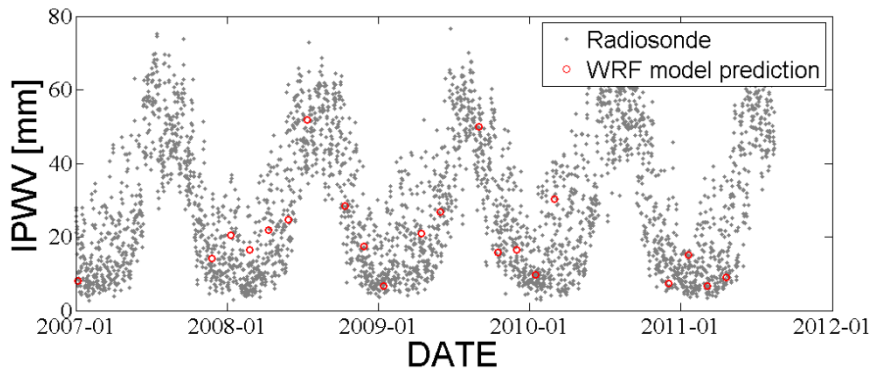


Fig. 15. Time series of the integrated precipitable water vapor (IPWV). The IPWV derived from the radiosonde data have a good agreement with that from the WRF model predictions.

Table. 5. Correlation coefficient and RMS error between vertical profiles of the radiosonde and WRF model

Date	Correlation Coefficient	RMS error
2007-11-25	0.9670	0.5471
2008-01-10	0.8544	1.4333
2008-02-25	0.8281	1.2875
2008-04-11	0.8322	1.3235
2008-05-27	0.9461	1.2427
2008-07-12	0.9590	1.7693
2008-10-12	0.9344	1.5202
2008-11-27	0.9424	0.9297
2009-01-12	0.9659	0.2658
2009-04-14	0.9534	1.7539
2009-05-30	0.8408	2.2312
2009-08-30	0.9600	1.7170
2009-10-15	0.9281	0.8855
2009-11-30	0.8870	1.0119
2010-01-15	0.9235	0.5983
2010-03-02	0.4145	3.1062
2010-12-03	0.9300	2.3012
2011-01-18	0.8647	0.7202
2011-03-05	0.9149	0.7119
2011-04-20	0.9191	0.6243

atmosphere such as temperature and air pressure. The second component means wet delay, atmospheric phase delay due to precipitable water vapor.

One advantage in using the WRF model is that it reflects realistic amount of water vapour regardless of cloud conditions unlike MODIS products. The limitation in using MODIS data were the lack of quantity of available data sets due to cloud coverage. However, it is possible to simulate meteorological conditions without cloud conditions in the WRF model.

In order to determine the accuracy of model results derived from WRF model simulation, a verification of the vertical accuracy is necessary. The vertical profiles of radiozonde were acquired at 00 UTC and 12 UTC every day. One radiozonde station (47827 Kagoshima Observations, Fig.8) is located in Kagoshima. It is reasonable that the collected radiosonde data reflect realistic and reliable conditions and could be used in the evaluation of the model simulations. The comparison of the atmospheric profiles of radiosonde data and those of the WRF model results in 2009-01-12 and 2009-08-30 shows the highest correlations (Fig. 14, Table5). The simulated integrated precipitable water vapour (IPWV) from the WRF model also has a capability of predicting the seasonality in this study area (Fig. 15).

Unfortunately, the comparison at other stations was not possible because there was only one radiosonde measurement station in the

coverage area of SAR data.

4.3. Results

4.3.1. Atmospheric correction using MODIS data

Unfortunately, the atmospheric correction using MODIS data was not sufficient for mitigation of all of the differential interferograms due to cloud cover. The qualified atmospheric correction was limited in a few differential interferogram. Fig.16 shows the results after the correction of atmospheric phase delay effects.

The fringe patterns in differential interferograms were present around Kirishima cluster (Shinmoedake). However, it is not easy to determine whether the fringe patterns represent the deformation by volcanic activity or errors, especially atmospheric phase delay, without fully understanding this volcano. The converted values of the atmospheric phase delay from precipitable water vapor in MODIS products show similar fringe patterns with differential interferograms around Kirishima cluster. Thus, the atmospheric information from MODIS can provide phase delay due to water vapor. The effects of water vapour are various depending on the acquisition time.

In case of the differential interferogram between 2008-05-27 and 2011-03-

05, the volcano inflated about 4 cm in the west of Karakunidake volcano with respect to the reference area (Fig. 16 A1). In Kirishima city, the undefined inflations were observed as well. The calculation of APS using MODIS data represents that the fringe patterns misinterpreted as the subsidence is present over Kirishima volcano cluster. After the correction, the fringe patterns are connected and distinct 4 cm inflation was measured in Karakunidake volcano and the inflations in Kirishima city were reduced (Fig. 16 A3).

Similar physical phenomena were found in the pair of 2008-05-27 and 2011-04-20 (Fig.16. B). Before the correction, the inflation in Kirishima city was present as well as in 2008-05-27 and 2011-04-05 while after the correction, these fringe patterns were mitigated. This implies that the inflation in Kirishima city might be artificial errors induced by atmospheric phase delay. It is worth noting that the distinct atmospheric phase delays calculated from MODIS data acquired at 2008-05-27, 2011-03-05, and 2011-04-20 are present in Kirishima city and the altitude of this region is relatively low. Therefore, this region is normally affected by the stratified APS. In Kirishima volcano, the stronger inflations (~ 5cm) were observed in the pair of 2008-05-27 and 2011-04-20 rather than in the pair of 2008-05-27 and 2011-03-05.

Based on this observation, ground deformation can be interpreted as the followings. 1) Ground inflates about 4~5cm with respect to 2008-05-

27. 2) Ground still inflated after the volcanic eruption. However, it does not mean that the deflation is not occurred after the eruption because this estimation tells only the ground deformation at the slave acquisition time with respect to the master acquisition time. 3) The inflation in Kirishima city is induced by APS.

Technically, the atmospheric correction using MODIS data can possibly mitigate the APS in differential interferograms. However, the lack of available dataset is the limitation in application of this technique due to cloud and different acquisition time between the MODIS data and SAR data.

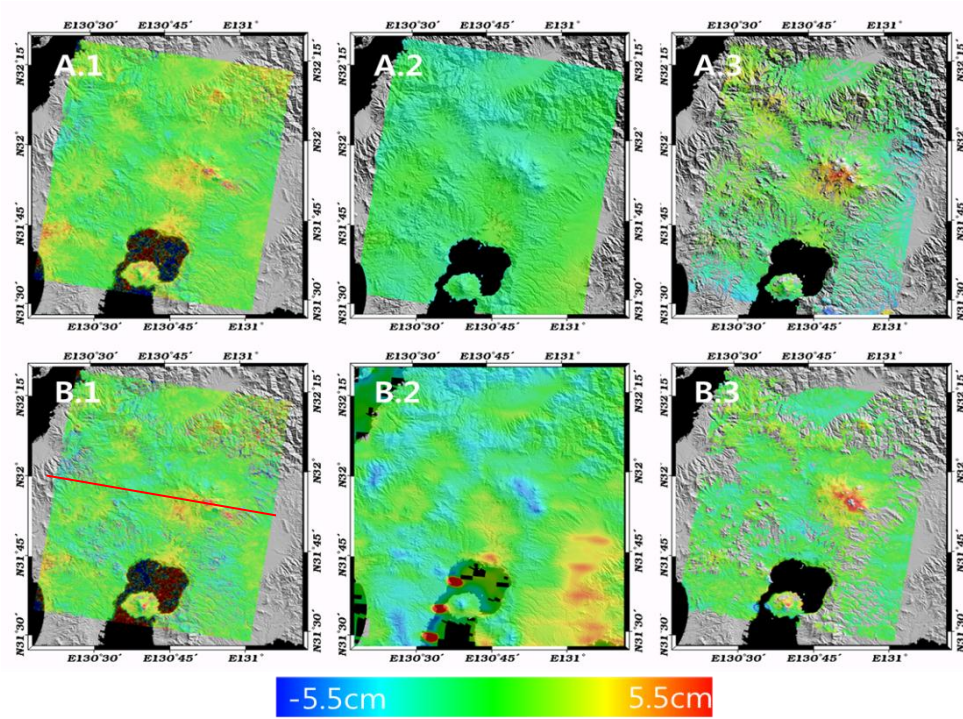


Fig. 16. Atmospheric correction using MODIS data. A.1. the uncorrected unwrapped differential interferogram from pair of 2008-05-27 and 2011-03-05 A.2. the atmospheric phase delay simulation using MODIS data A.3. the atmosphere corrected differential interferogram B.1. the uncorrected unwrapped differential interferogram from pair of 2008-05-27 and 2011-03-05 B.2. the atmospheric phase delay simulation using MODIS data. B.3. the atmosphere corrected differential interferogram

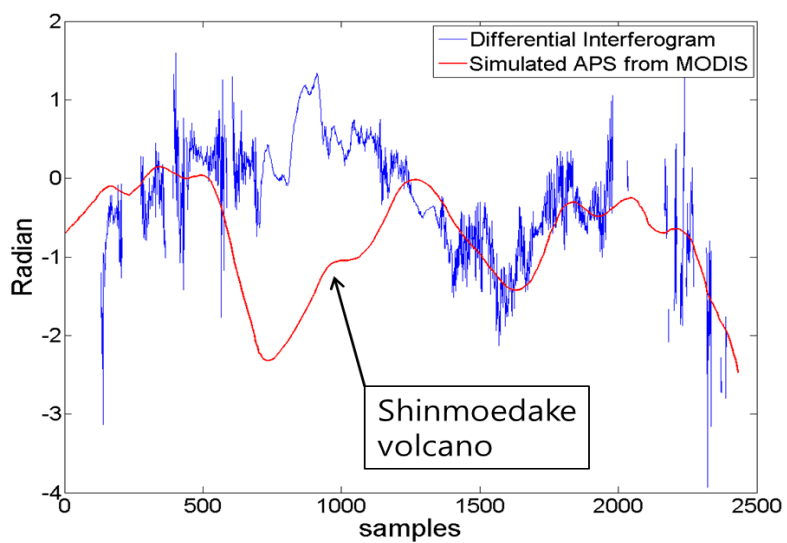


Fig. 17. Comparison of differential interferogram and simulated APS from MODIS generated from a pair of 2008-05-27-2011-04-20 across the red line in Fig.16.

4.3.2. *Atmospheric correction using WRF model*

For a spatial comparison, the simulated APSs from the WRF model were compared to a differential interferogram which has small temporal baseline (Fig. 18). Because the time interval of this interferogram is only 45 days, the assumption that the ground deformation is ignorable is reasonable. Under the assumption that every fringe pattern comes from APSs, the simulated APSs have to have high correlation with the differential interferogram. Fig.18 shows the spatial distribution of APS in each differential interferogram and the simulated APS. The results give good agreements in the pairs of 2009-01-12 and 2009-04-14, 2009-08-30 and 2009-10-10, and 2008-02-25 and 2008-04-11. The distinct agreements are usually found in the volcano, mountains, and Kirishima city. It means that the stratified APS could be predicted using the WRF model. However, several regions show disagreements. These errors can be explained from a different spatial resolution and difficulties in simulation of the turbulent APS.

The spatial resolution of the WRF model is 1 x 1 km while the multi-looked differential interferograms are 28 m x 18 m. A reliable simulation procedure using the WRF model is possible over 1 x 1 km nested domain. Therefore, the spatially small scaled APS cannot be simulated using the WRF model. The filtered differential interferograms can reflect the small-

scaled and large-scaled APS. It means that differential interferograms could reflect the meteorological condition of high spatial resolution.

Secondly, the WRF model predicts the meteorological conditions using reanalysis dataset (6 h FNL dataset in this study), however, the turbulent APS usually occur randomly in time. The modeling of meteorological data is a basis of the meteorological dynamics. Since the WRF model use temporally less dense datasets, it might predict only the temporal correlated meteorological conditions

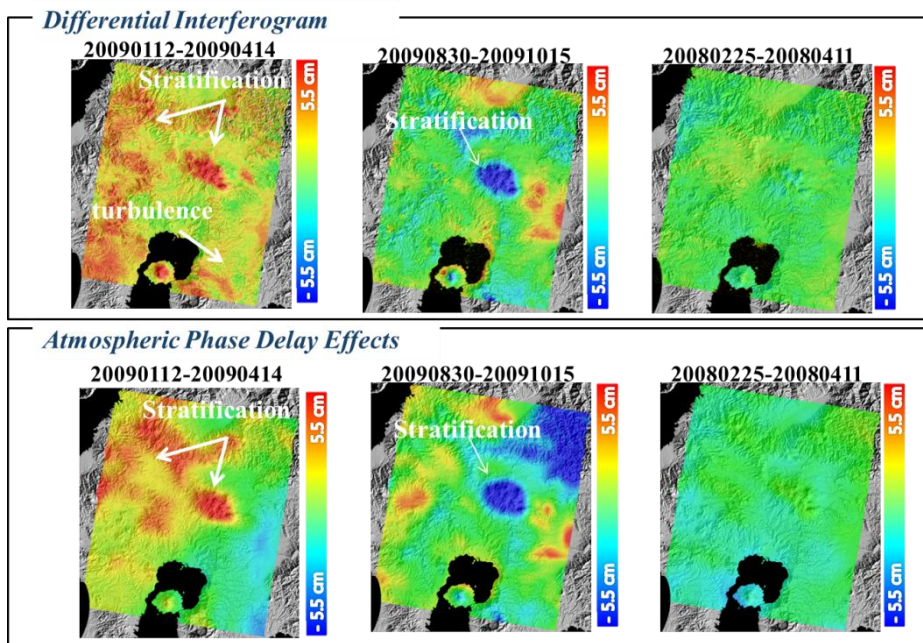


Fig. 18. Comparison of differential interferograms and simulated atmospheric phase delay using WRF model. The selected differential interferograms have the 46 days interval. So, the ground deformation can be ignorable.

5. Atmospheric correction using time-series analysis

To understand the volcanism, the change of magma storage, migration and magma supply information are required. Time series analysis of differential interferograms enables the identification of the pattern of ground deformation. Generally, the Persistent Scatterers SAR Interferometry (PSInSAR) and Small BAseline subset algorithm (SBAS) have been applied to various phenomena [A. Ferretti et al., 2000; P. Berardino et al., 2002].

SBAS algorithm basically utilizes only differential interferograms which have relatively small perpendicular baseline to minimize decorrelation. SBAS algorithm links differential interferograms using singular value decomposition (SVD) and measures ground deformation. The main idea to detect and remove the atmospheric phase component from the time-series phase is similar as used in PSInSAR. PSInSAR, and SBAS assume that the atmospheric phase delay effects exhibit a significantly low temporal and spatial correlation. In this respect, both algorithms mitigate the atmospheric phase delay effects using low pass filtering in space and time. However, reconsideration of this assumption is required, especially whether the atmospheric phase delay effects uncorrelated in time or not. To identify the characters of the atmospheric

phase delay effects, the residuals of the atmospheric phase delay effects were estimated after SBAS algorithm and PSInSAR are applied. In this study, StaMPS algorithm and the enhanced SBAS were applied to this research.

5.1. APS estimation errors in time-series InSAR

After selection of the PSs in each differential interferogram and unwrapping in StaMPS, each unwrapped differential interferogram can be describes as following [A. Hooper, 2006]:

$$\phi_{uw} = \phi_{def} + \phi_{atm} + \Delta\phi_{orb} + \phi_{\theta} + \Delta\phi_n \quad (45)$$

where ϕ_{uw} is unwrapped differential interferograms, ϕ_{def} is ground deformation. ϕ_{atm} , ϕ_{orb} , ϕ_{θ}^{corr} and $\Delta\phi_n$ are atmospheric contribution, residual orbital ramps, DEM error and random noise, respectively. The APS can be defined as the difference between the master APS and the slave APSs. The master APS is involved in every differential interferogram. To estimate the master contribution of APS and orbital ramp, low pass filtering can be carried out because this contribution is involved in every differential interferogram. After low pass filtering, the residuals of differential interferograms consist of ground deformation and the master contribution of the APS and orbital ramps.

$$\mathcal{L}^T\{\phi_{uw}\} \approx \phi_{def} - \phi_{atm}^m - \Delta\phi_{orb}^m \quad (46)$$

where \mathcal{L}^T is low pass filtering operator in time, and the superscript m denotes master contribution to each term. In the master SAR images, ground deformation could be set as zero and it yields the master contribution of APS and orbital ramps. The slave contribution of APS and orbital ramps can be obtained by subtracting the residuals of low pass filtering from unwrapped differential interferograms.

$$\phi_{uw} - \mathcal{L}^T\{\phi_{uw}\} = \phi_{atm}^s + \Delta\phi_{orb}^s + \Delta\phi_\theta + \Delta\phi_n \quad (47)$$

Generally speaking, the spatial filtering can be an effective way to alleviate noises in each differential interferogram because the noises are present as a Gaussian distribution. As a result, eq.45 can be rearranged and ground deformation can be estimated from subtracting the estimated errors.

$$\phi_{def} \approx \phi_{uw} + \widehat{\phi_{atm}^m} - \widehat{\phi_{atm}^s} - \widehat{\Delta\phi_{orb}^s} - \widehat{\Delta\phi_\theta} - \Delta\phi_n \quad (48)$$

where $\widehat{\phi_{atm}^m}$, and $\widehat{\phi_{atm}^s}$ are the estimated master and slave APS. $\widehat{\Delta\phi_{orb}^s}$ is the estimated orbital errors in slave images. $\widehat{\Delta\phi_\theta}$ is the estimated DEM error.

However, the assumption about APS proposed in StaMPS might be invalid because water vapor contents, pressure, and temperature have seasonality and APS can be explained as the sum of correlated and uncorrelated APS in time. Simple experiments for the estimation of residual APS were carried out. On this purpose, differential interferograms with only APS were generated from the estimated atmospheric phase delay dataset from WRF model predictions. If the contribution of the residual

APS do not exist or is ignorable, it should be mitigated after time-series analysis such as PSInSAR and SBAS.

In Fig.19 and Fig. 20, the phase values represent the residuals of APS after processing SBAS and PSInSAR algorithm, respectively. Basically, the conventional time-series analyses estimate temporally uncorrelated phases and define them as APS. Even though time-series InSAR approaches were applied with the differential interferograms, the residual phases remain and could be misunderstood as a ground deformation. In other words, the residual APS can be misinterpreted as ground deformation. Since the residuals are usually located in mountain i.e. volcano, an assumption that the stratified atmospheric phase delay effects are mainly associated with the residual APS is valid. The contributions of the stratified atmospheric phase delay in differential interferograms severely contaminate small scaled ground deformation at volcano. Eq.46 and eq.47 should be rewritten following after low pass filtering.

$$\mathcal{L}^T\{\phi_{uw}\} \approx \phi_{def} - \phi_{atm}^m - \Delta\phi_{orb}^m + \phi_{res.atm} \quad (49)$$

$$\phi_{uw} - \mathcal{L}^T\{\phi_{uw}\} = \phi_{atm}^s - \phi_{res.atm} + \Delta\phi_{orb}^s + \Delta\phi_{\theta} + \Delta\phi_n \quad (50)$$

where $\phi_{res.atm}$ is residual APS in slave images.

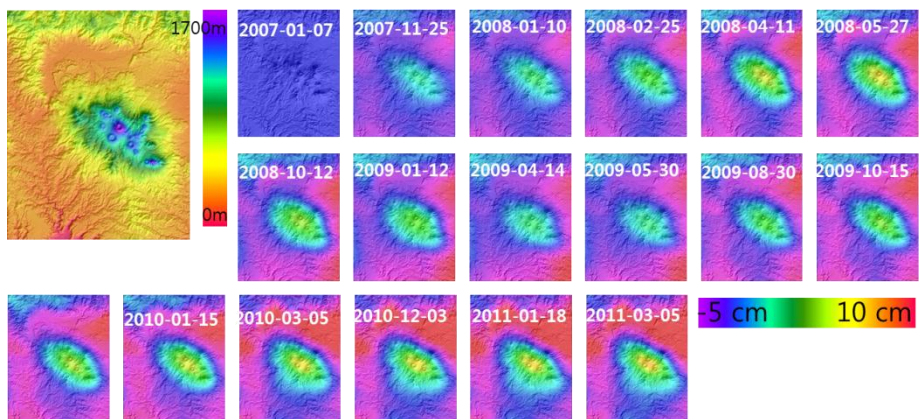


Fig. 19. Residual APS after processing SBAS.

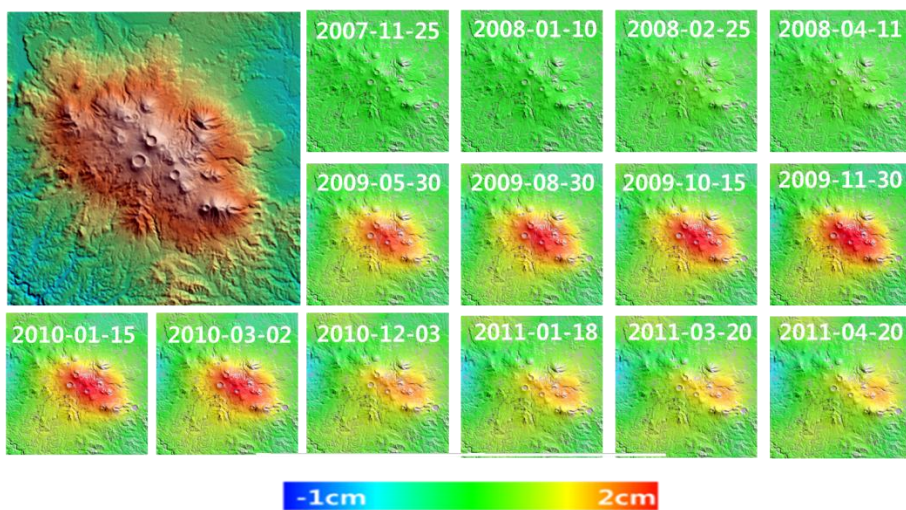


Fig. 20. Residual APS after processing PSInSAR algorithm.

5.2. Properties of APS in time and space

It is necessary to identify and measure what properties of APS yield the residual APS and how the residual APS affects the quality of differential interferograms. For this, several scenarios were set; 1) differential interferograms have only ground deformation, 2) differential interferograms have ground deformation with the stratified APS, 3) differential interferograms with ground deformation and the turbulent APS.

5.2.1. *Volcanic deformation model*

Ground deformation was modeled based on GPS displacement measurement. The Japanese Meteorological Agency (JMA) has observed the volcanic activities in Shinmoedake volcano using continuous GPS stations. Three continuous displacement measurements located on Shinmoedake volcano can be applied into this modeling. The volcanic model enables the conversion from 3-dimensional displacement at one point to 3-dimensional displacement over the area. Mogi model is an effective model to simulate the ground deformation caused by volcanic activities, since a few parameters such as volume change, depth, and horizontal location of magma chamber are required [K. Mogi et al.,1958].

To model more distinct volcanic deformation, the six-month

displacement measurements are used. Under the assumption that the magma source is located beneath Shinmoedake volcano at 3.4 km depth, the volume changes of magma chamber using GPS measurement were derived. Mogi model can compute the horizontal and vertical displacement caused by changes of hydrostatic pressures of a spherical source assuming a homogeneous and semi-infinite elastic body.

$$\Delta h = \frac{3f}{4\pi r^3} \Delta V, \quad \Delta l = \frac{3d}{4\pi r^3} \Delta V \quad (51)$$

where Δh and Δl are the vertical and horizontal displacement, respectively. The r is the distance between the source and the measurement point. f and d are the depth of the center of a spherical source and the horizontal distance from a spherical source to the measurement point, respectively. ΔV is the volume change of a spherical source. By using singular value decomposition of the x-, y-, z- direction displacements measured by 3 GPS station, the volume changes were computed from 2007 to 2011. The simulated x-, y-, z- direction displacements are converted to the line of sight displacement corresponding to the SAR acquisition time. The model results reflect the realistic nonlinear deformation in Shinmoedake volcano.

5.2.2. *Decomposition of APS*

The stratified atmospheric phase delay effects have relation with height. The atmospheric decomposition of APS can be achieved based on

the topographic information. Simply, the stratified APS can be obtained by eq.52

$$\phi_{\text{atm}} = a \times \text{dem} + b \quad (52)$$

However, the topographic height in this study area varies from 0m to 1700m. Naturally, the thick atmospheric stratification can be expected. For better decomposition of APS, the validation of above equation is required. Precipitable water vapor in columns was integrated at each height using the vertical profile of radiosonde. Fig.21 shows that the integrated precipitable water vapor (IPWV) at each height can be expressed better as a 2nd-order polynomial of height than as a 1st-order polynomial in most cases. Therefore, the estimation of the stratified APS of the WRF model results can be decomposed using the following equation.

$$\phi_{\text{atm}} = a \times \text{dem}^2 + b \times \text{dem} + c \quad (53)$$

5.2.3. *Model results*

Every scenario was carried out using StaMPS. In each scenario, the time windows were set as 2 years, 1 year, and 6 month for the temporal weighted low pass filtering.

According to the model simulation results, as increasing the temporal filter window size, the ground deformations are smoothed. It is hardly recognized that the smoothed ground deformation by low pass filtering in

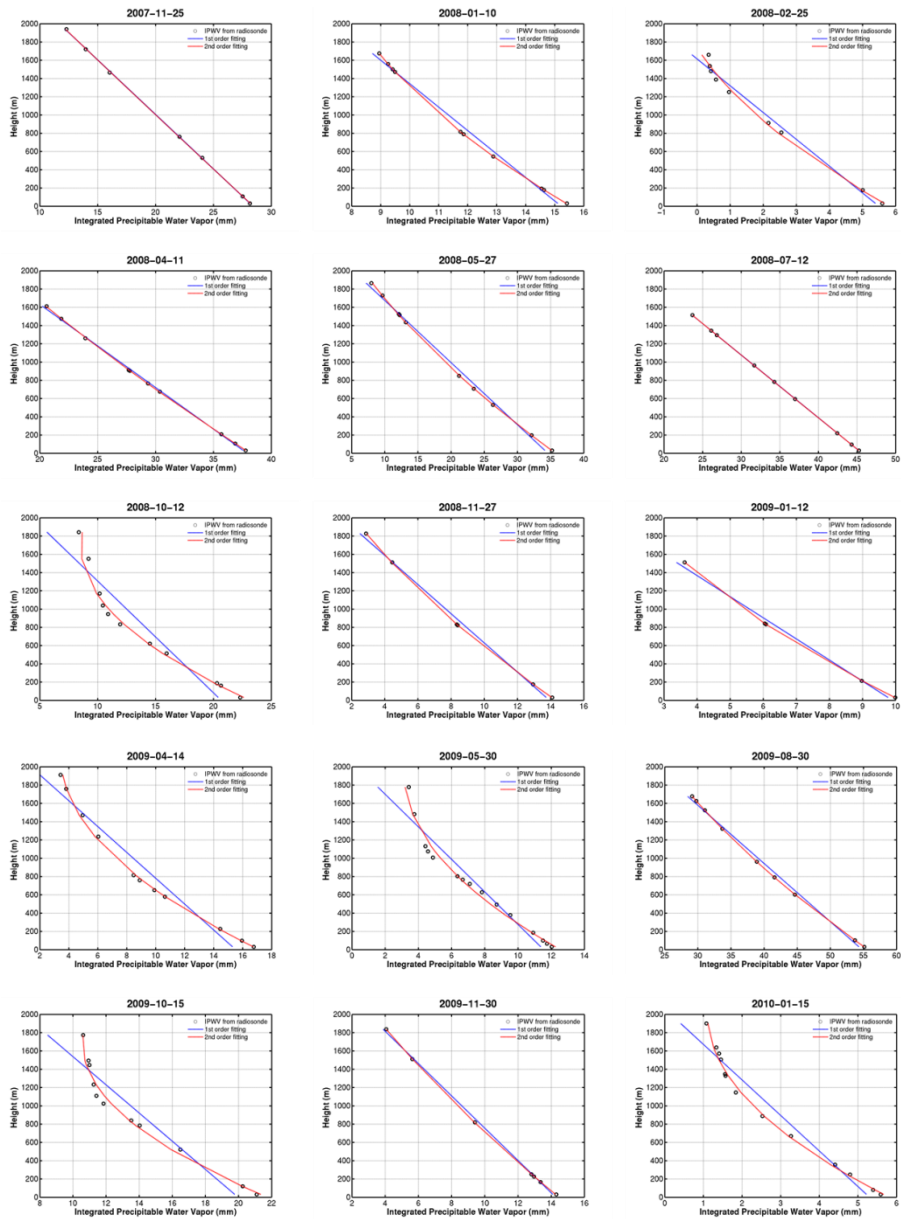


Fig. 21. Stratified APS estimation method. The precipitable water vapor profiles measured by Radiosonde were integrated in column at each height. Blue line means the linear fitting with height and red line is the 2nd order fitting.

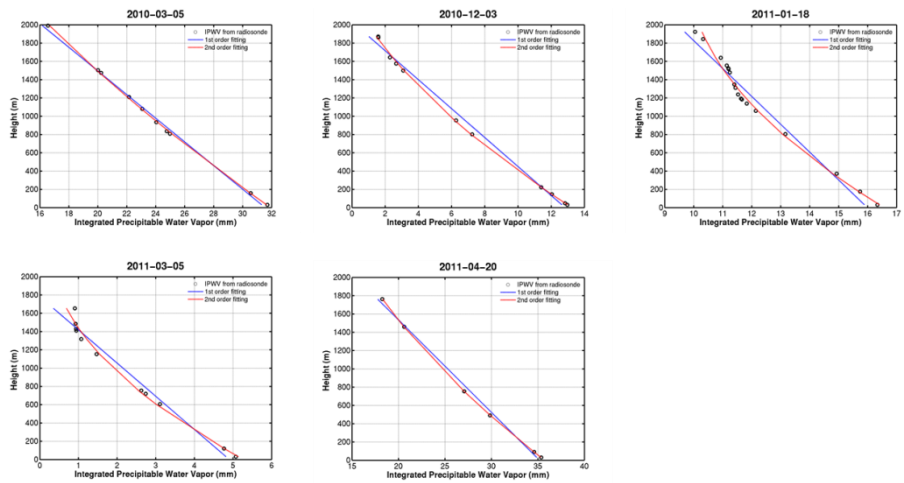


Fig. 21. continued

time of 730 and 365 days are the same with the reference ground deformation estimated from the deformation model. In Fig.22.b and Fig.23.b, the turbulent APS was added to the simulated ground deformation. As increasing the time window size, the residuals are smoothed. It means that the turbulent APS randomly occurs at SAR acquisition time and can be successfully mitigated with low pass filtering as suggested in PSInSAR, SBAS method and stacking method if datasets are sufficient for the turbulent APS to converge to zero. In contrast to the turbulent APS, ground deformation is still affected by low-frequency of the stratified APS by using only temporal low pass filtering because the stratified APS is vertically variable and is not generated randomly, but seasonal as in Fig.22.c and Fig.23.c. Thus, low pass filtering method is less efficient to mitigate the stratified APS than the turbulent APS.

For the mitigation of the stratified APS from the atmospherically uncorrected differential interferograms, two different approaches are possible. The first is the direct estimation of the stratified APS from differential interferograms and geometric data. The second is the atmospheric decomposition from auxiliary meteorological data, the WRF model in this study. However, the accuracy of the first approach absolutely depends on the quality of differential interferograms. Even though differential interferograms give high coherence, the method can be limited in volcanic areas since the ground deformation induced by volcanic

activities can be located in the summit as a function of height. Fig.24 shows the comparison of two approaches in the experiments, and the estimation error of the stratified APS due to the ground deformation in 2010 yields additional ground deformation errors. Therefore, to measure ground deformation accurately, additional use of auxiliary data can be one of the most efficient solutions for correction of the stratified APS.

The above ground model and APS simulation have the following implications;

- 1) In volcanic areas, time-series analysis still has the residuals of APS and those effects are mainly induced by the stratified APS.

- 2) The method using geometric data and differential interferograms for calculating the stratified APS might yield additional errors due to topographically related ground deformation.

- 3) The stratified APS estimation using meso-scale weather forecasting models is effective and it could reduce the stratified APS in differential interferograms. The turbulent APS can be mitigated applying low pass filtering in the conventional time-series analysis.

According to these model results, more reliable estimation method for APS can be modified in time-series analysis. In Fig.25 after PS selection, the wrapped phase will be corrected using the stratified APS estimated from the WRF model. In this step, the determinant stratified APS might be mitigated as mentioned in the simulation results. In the case of the

turbulent APS, low pass filtering method in time can mitigate the amplitude of temporally uncorrelated APS. The phases after subtracting the turbulent APS estimated from low pass filtering and the stratified APS simulated from the WRF model are mainly related to ground deformation. Additionally, the sum of the stratified APS and the estimated turbulent APS reflect real APS at SAR acquisition time.

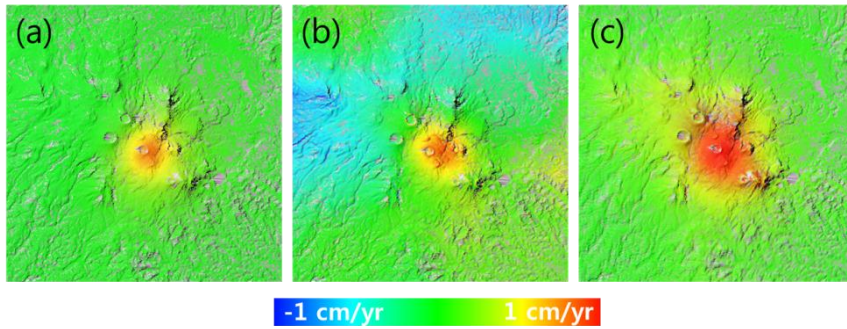


Fig. 22. Mean velocity (cm/yr) of simulated ground deformation. (a) Simulated ground deformation. (b) Simulated ground deformation and estimated turbulent APS (c) Simulated ground deformation and estimated stratified APS. In mean velocity map, turbulent APS seems to affect the ground deformation. However, it does not mean the variation of turbulent APS is large. In the same respect, the stratified APS can affect severely the ground deformation in time series analysis.

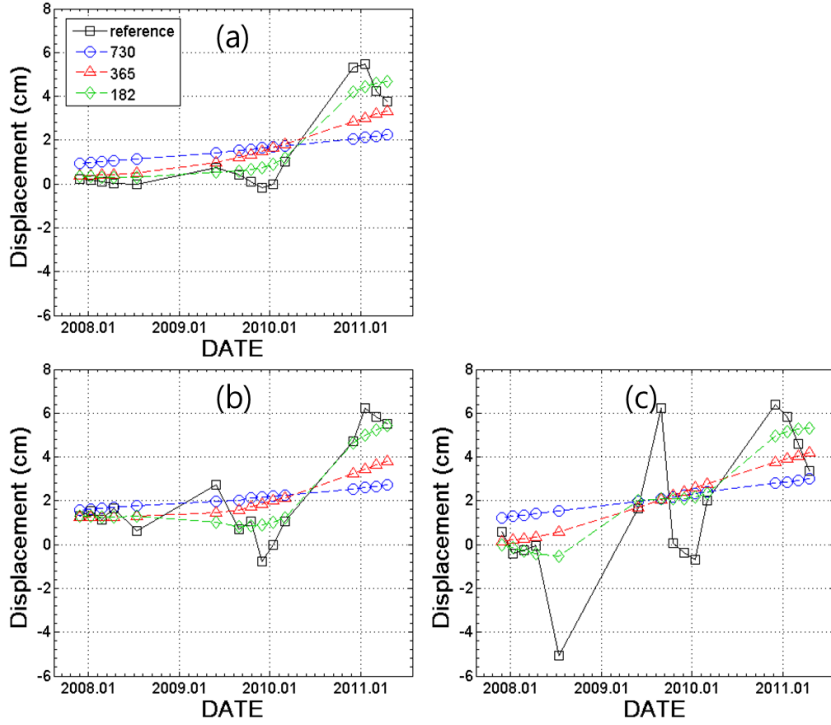


Fig. 23. Time series analysis with time window 720, 365, 243, 182, and 146 days

for temporal low pass filtering. (a) The time series of the simulated ground deformation. (b) The time series of simulated ground deformation and estimated turbulent APS (c) Time series of simulated ground deformation and estimated stratified APS

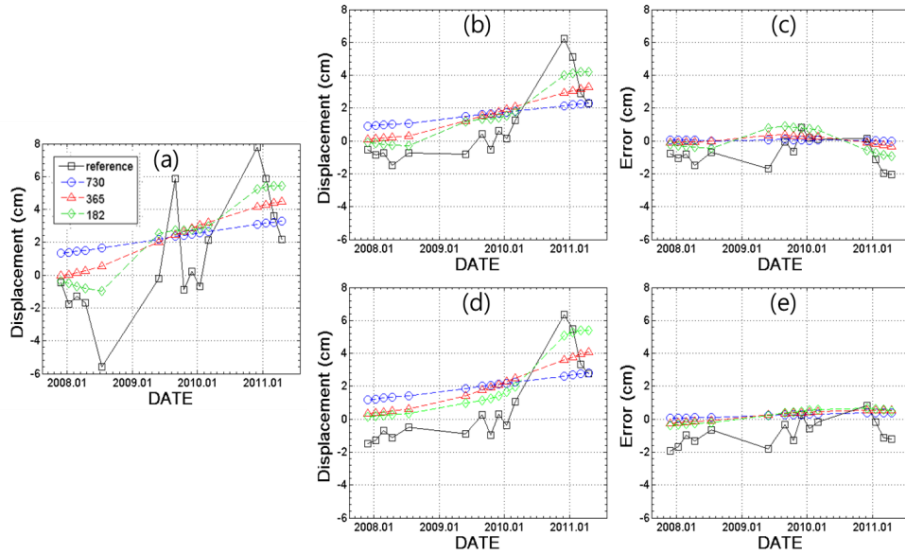


Fig. 24. Time series plots of the sum of ground deformation and total APS (a), after atmospheric correction using stratified APS estimated from WRF model (b), after atmospheric correction using stratified APS estimated from simulated differential interferograms (c), residual of two approaches (d), (e). In every approach, low pass filtering method was applied with 730, 365 and 182days.

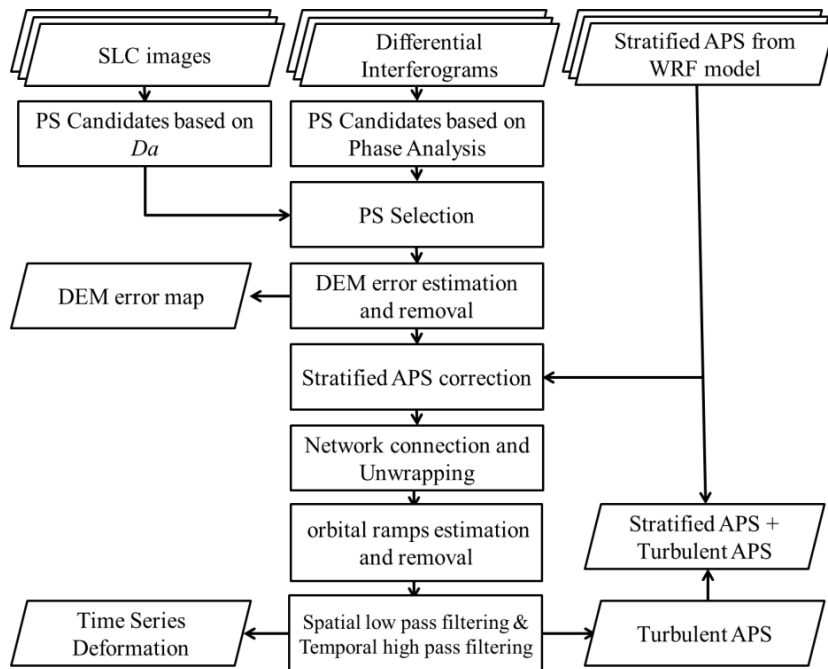


Fig. 25. Flow chart of atmosphere corrected PSInSAR

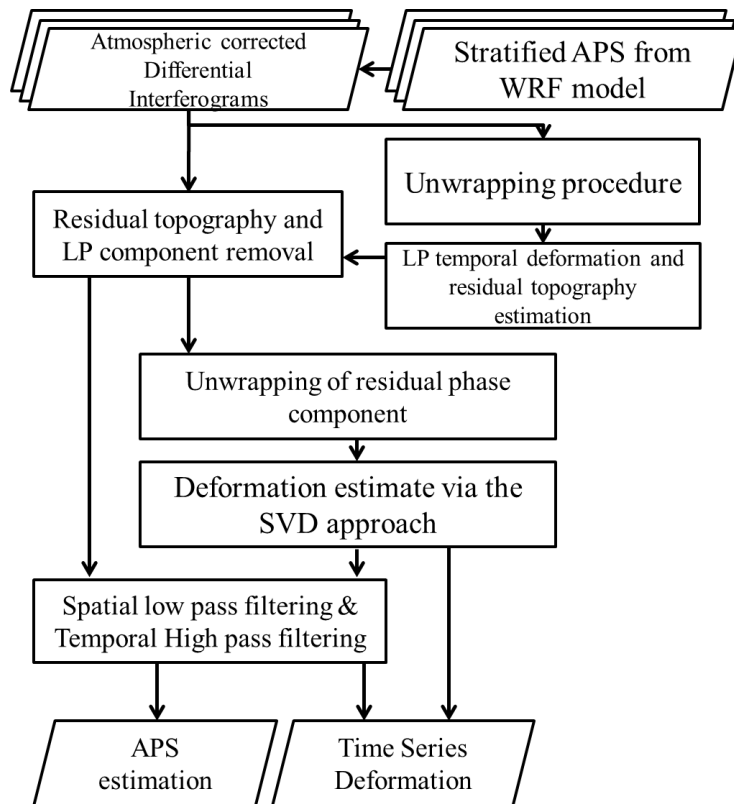


Fig. 26. Flow chart of atmosphere corrected SBAS

5.3. Application to available dataset and data processing

Table 6 and table 7 show available ALOS PALSAR images in 4 years involving the volcanic eruption event in 2010 for SBAS and PSInSAR, respectively. The interferometric pairs were selected based on the perpendicular and temporal baseline. The critical baseline for SAR interferograms generated from ALOS PALSAR is approximately 13 km. The interferometric pairs with the perpendicular baselines (3120m, in this study) below the critical baseline are all available in PSInSAR algorithm. In the case of SBAS, the pairs with small baselines (1300m in this study) are recommended due to geometrical decorrelations. The topographic contributions were removed using SRTM DEM (90 x 90 m resolution). The SLC image in 2008-05-28 was selected as the master image for PSInSAR. Total 49 and 15 interferograms were obtained for SBAS and PSInSAR, respectively.

The criterion for selecting reliable pixels for SBAS was coherence. The coherence values below 0.2 were masked out. For PSInSAR, the PS selection method of StaMPS was applied. After the PS selection in StaMPS algorithm, 1.5% of all pixels were identified using amplitude dispersion of SLC images and phase analysis. The DEM errors were calculated iteratively and the maximum DEM error was 15 m. The mean

of the DEM error is only 0.01 m. For atmospheric correction, the derived stratified APS derived from the WRF model were corrected in each wrapped differential interferogram to avoid the unwrapping problem possibly induced by APS. The turbulent APSs in each slave image were estimated using low pass filtering of 180 days in time. The differential interferograms had the stratified APS and turbulent APS before applying the suggested method. Fig.27 shows that the unwrapped phase before the atmospheric correction was correlated with height. The estimated stratified APS from the WRF model have a good agreement with the phase in the area except Shinmoedake volcano as in Fig.28. However, in Shinmoedake volcano, the ground deformation cause by the volcanic activity in 2010 is involved and this disagreement can imply the ground deformation. Therefore, the estimation of the stratified APS is valid and reliable.

Table 6. Available ALOS PALSAR pair for SBAS.

Number	Pair	Perpendicular	Temporal
	(master-slave)	baseline (m)	baseline (days)
1	20070107-20071125	-16.4	322
2	20070107-20080110	233.6	368
3	20070107-20080225	409	414
4	20070107-20100302	-165.3	1150
5	20071125-20080110	198.9	46
6	20071125-20080225	776.7	92
7	20071125-20100302	-144.7	828
8	20080110-20080225	177.4	46
9	20080110-20100115	-410.9	736
10	20080110-20100302	-307.32	782
11	20080225-20080411	210	46
12	20080225-20080527	384.6	92
13	20080225-20101203	495.2	1012
14	20080225-20110118	756.1	1058
15	20080411-20080527	235.3	46
16	20080527-20080712	-1142.6	46
17	20080527-20101203	-137.2	920
18	20080527-20110118	128	966
19	20080527-20110305	252.5	1012
20	20080712-20081012	-554.8	92
21	20080712-20090414	-269.9	276
22	20080712-20090530	106.3	322
23	20080712-20090830	-281.6	414

24	20080712-20091015	43.5	460
252	20080712-20091130	252.8	506
26	20080712-20100115	463.7	552
27	20081012-20081127	136.8	46
28	20081012-20090112	247.1	92
29	20081127-20090112	301.5	46
30	20090112-20090414	394.2	92
31	20090112-20090830	624.1	230
32	20090414-20090530	633.7	46
33	20090414-20090830	135.8	138
34	20090414-20091015	277.4	184
35	20090414-20091130	868.2	230
36	20090530-20090830	-380.9	92
37	20090530-20091015	-68.9	138
38	20090530-20100115	642.4	230
39	20090830-20091015	326.4	46
40	20090830-20091130	484.6	92
41	20091015-20091130	218	46
42	20091015-20100115	668.5	92
43	20091130-20100115	258.6	46
44	20091130-20100302	748.9	92
45	20100115-20100302	178	46
46	20100302-20101203	1372.7	276
47	20101203-20110118	202.2	46
48	20110118-20110420	824.9	92
49	20110305-20110420	230.2	46

Table 7. Available ALOS PALSAR dataset for PSInSAR.

Image	Date	Temporal	Perpendicular
Number	(YYYYMMDD)	baseline (days)	baseline (m)
1	20071125	-184	-1390
2	20080110	-138	-1069
3	20080225	-92	-604
4	20080411	-46	-398.65
5	20080527	Master	
6	20080712	46	-2687
7	20090530	368	-2574
8	20090830	460	-3120
9	20091015	506	-2632
10	20091130	552	-2347
11	20100115	598	-1881
12	20100302	644	-1522
13	20101203	920	-125
14	20110118	966	146
15	20110305	1012	500
16	20110420	1058	988.64

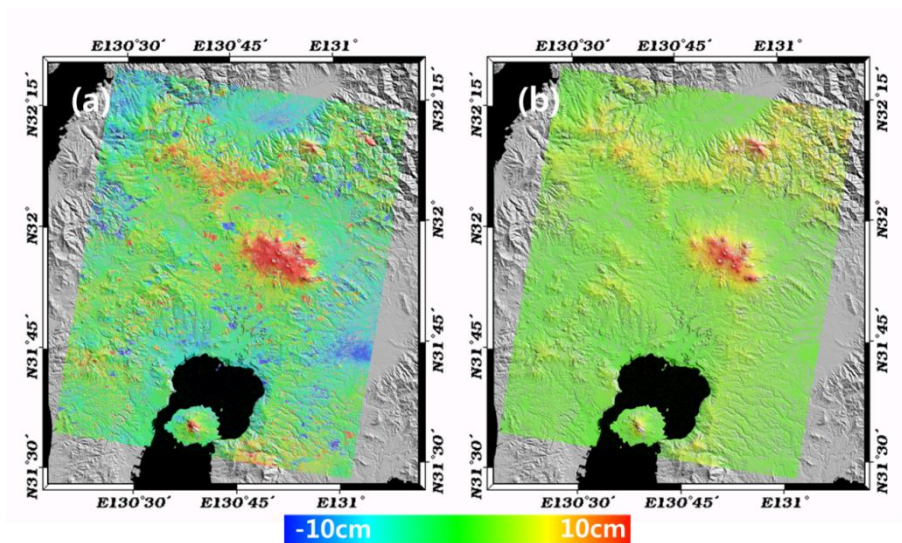


Fig. 27. (a) Differential interferogram from pair between 2008-05-27 and 2009-10-15 and (b) estimated stratified APS corresponding to the same date

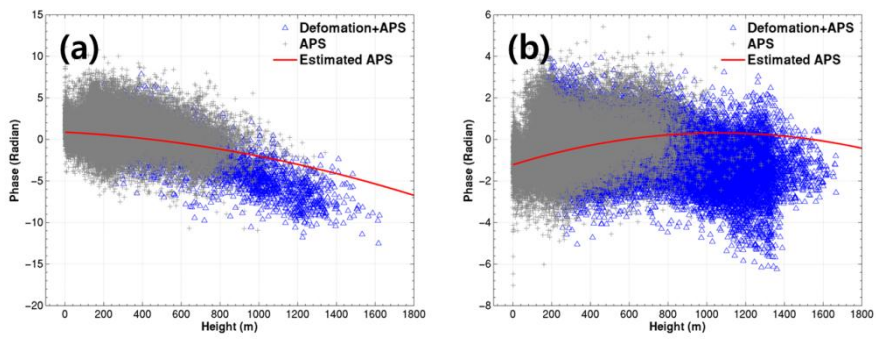


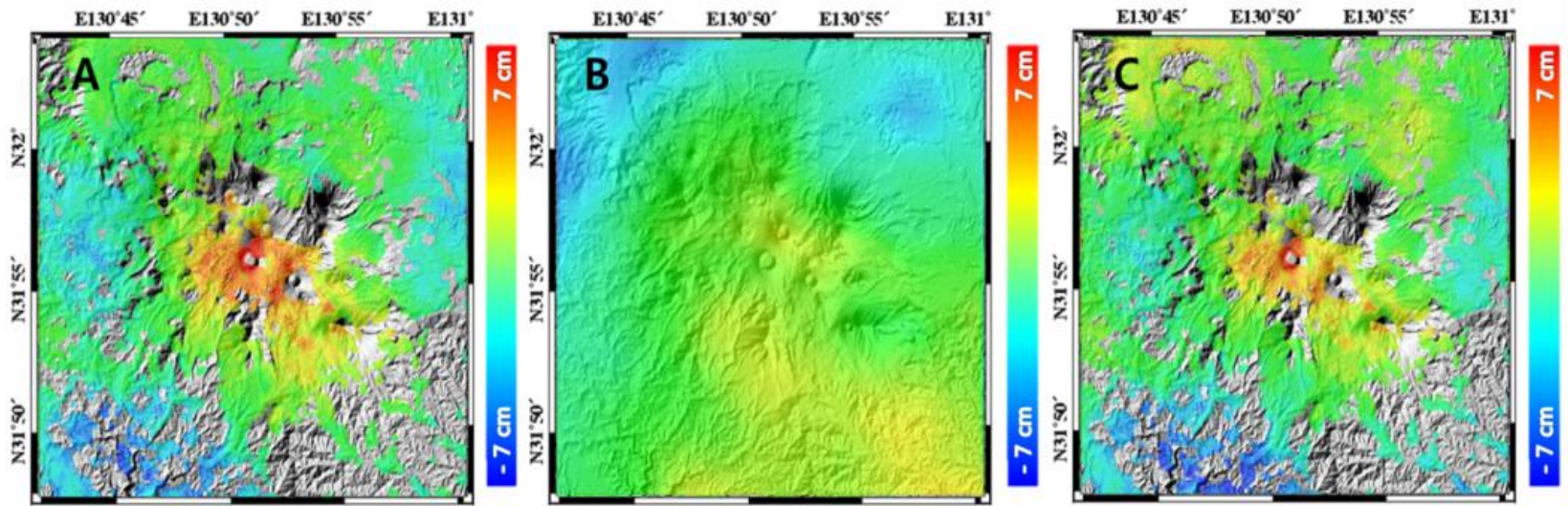
Fig. 28. Scatter plot of unwrapped phase of Ifms and height between 2008-05-27 and 2009-10-15 (a) and 2008-05-27 and 2011-03-05 (b). Blue triangles are the phase in Shinmoedake volcano and gray crosses represent the phase in the region except Shinmoedake volcano. Red line is estimated APS from WRF model.

5.4. Comparison between conventional and atmosphere corrected time series analysis

5.4.1. *Atmosphere corrected SBAS*

The displacements at the volcano summit were measured to analyze the deformation pattern. The conventional SBAS without atmospheric correction shows uplifts in 2010 (Fig. 27 A). Before the atmospheric correction of SBAS, the results represent the volcanic deformation and residual of the APS. After simulation of APS, the residual APS were approximately 2cm/yr in 2010. Therefore, after the atmospheric correction, 3~4cm/yr inflation occurred in 2010 in Shinmoedake volcano.

The atmospheric technique used in this study has several advantages in volcanic deformation measurement. First, the simulated atmospheric phase delay effects accurately reflect real atmospheric condition and reduced the artifacts in interferograms. In particular, the stratified atmospheric phase delay effects can be successfully mitigated. Secondly, more accurate time-series surface displacement analysis is possible.



1

2 Fig. 29. A. ground deformation rate (cm/yr) in 2010 measured by conventional SBAS. B. simulated atmospheric phase delay effect rate(cm/yr) in 2010. C.

3 Atmosphere corrected ground deformation rate (cm/yr) calculated by proposed method.

5.4.2. *Atmosphere corrected PSInSAR*

The main conceptual difference between the conventional PSInSAR (i.e. StaMPS) and the atmosphere corrected PSInSAR is the assumption of atmospheric properties. The conventional PSInSAR expects that the atmosphere is inhomogeneous in time whereas the proposed method assumes that the APSs contained in differential interferograms consist of the temporally uncorrelated APS relevant to the turbulent APS and the residual APS mainly associated with the stratified APS. The atmosphere corrected PSInSAR firstly estimates the stratified APS which can be significant and corrected by using the WRF model. Then, the turbulent APS is reduced in time-weighted low-pass filtering. This approach has an advantage of mitigating the small scaled displacement induced by the atmosphere and topography and extracting more accurate volcanic ground deformation in a basis of physical and seasonal properties of the atmospheric errors. Fig. 30 and Fig.31 represent the estimated ground deformation in Shinmoedake volcano from the conventional methods and the suggested method, respectively. According to the ground deformation from StaMPS, Shinmoedake inflated from 2009-05-30 to 2009-08-30 and from 2010-12-03 to 2011-01-18. In 2009, Shinmoedake volcano reached the maximum ground deformation rather than in 2010, however, GPS measurement and the simulated ground deformation (Fig. 23.a) show that

the significant inflation was observed in 2010. It is worth noting that the estimated residual APS is reaching the maximum in 2009. Thus, this unexpected ground deformation in 2009 can be interpreted as the residual APS effects. In Fig.30, the residual APS was reduced and the maximum inflation caused by volcanic activities was observed in 2010. This results support that the suggested method can mitigate the residual APS and improve the accuracy of ground deformation.

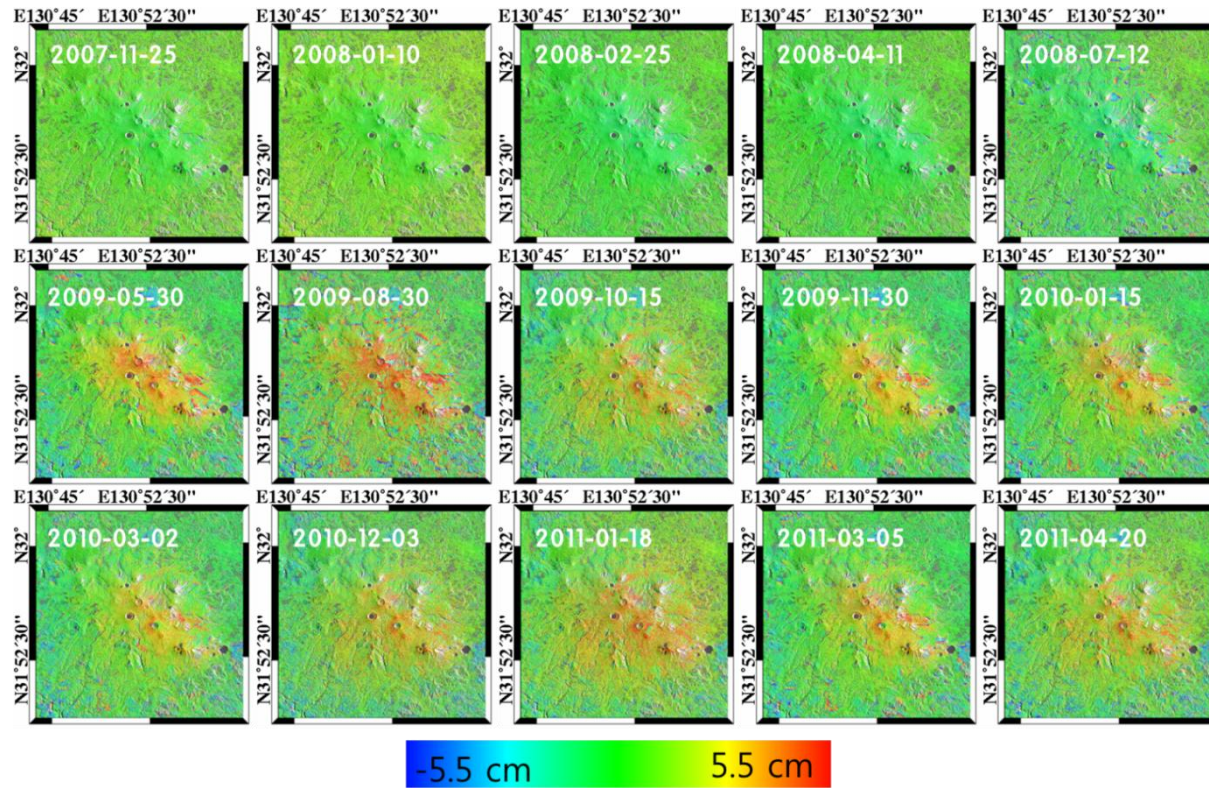


Fig. 30. Ground deformation measured from conventional PSInSAR (StaMPS). Maximum value of ground deformation is shown at 2009-08-30

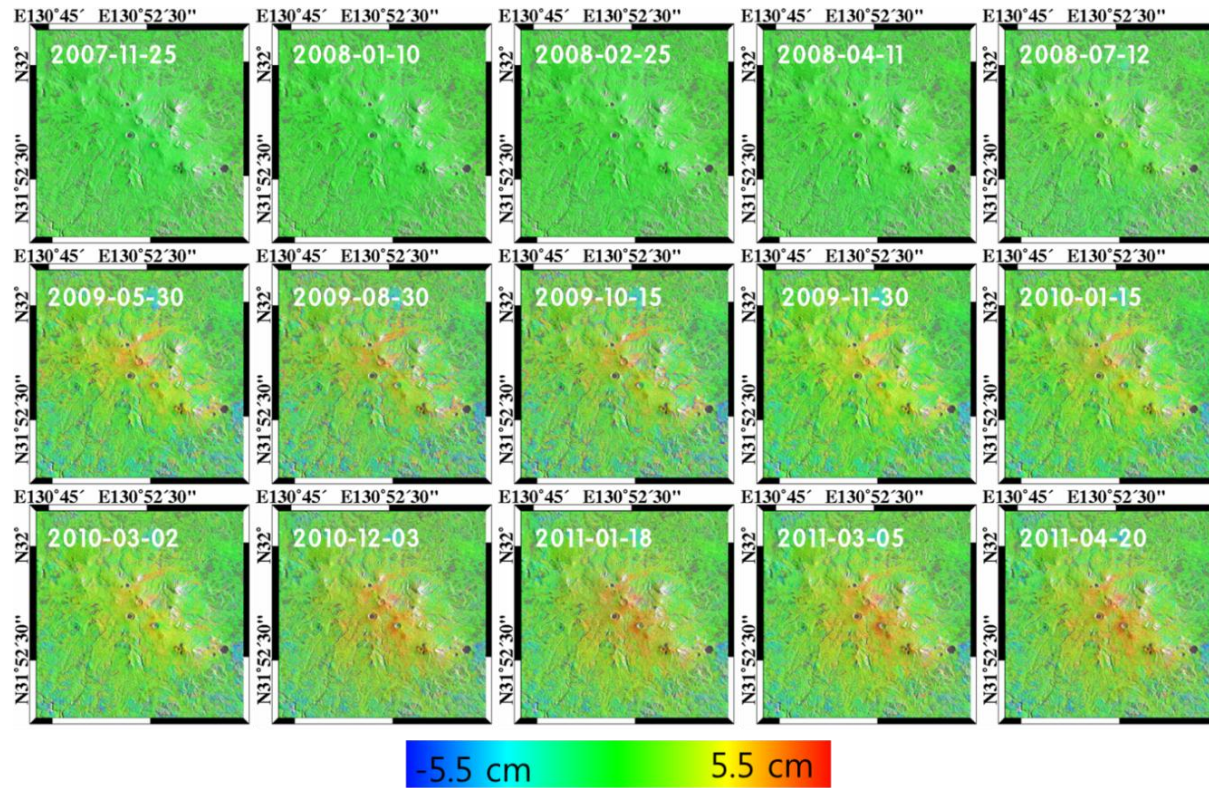


Fig. 31. Ground deformation measured from atmosphere corrected PSInSAR (StaMPS).

5.5. Validation

In order to validate the results, several tests were performed. The first validation approach is the comparison of the line of sight displacement measured by GPS stations and the estimated ground deformation from the conventional and the atmosphere corrected methods. The x-,y- and z-displacement of GPS is projected to the LOS for comparison.

The results show that the displacement trends in the atmosphere corrected SBAS approach are more similar and closer with the displacements from GPS in the LOS directions than those in SBAS without the atmospheric corrections (Fig. 32). The standard deviation of the time-series algorithm with the atmospheric correction is smaller than the conventional SBAS algorithm which uses only HP filter and LP filter for atmospheric correction. Thus, the presented methods can be an appropriate method for the measurement of surface displacements.

In Fig. 33, the estimated ground deformations from the conventional and the atmosphere corrected PSInSAR are compared. At locations of two GPS stations, the atmosphere corrected PSInSAR gives closer ground deformation respect to the reference ground deformation (GPS) than the conventional method. The rms error between the measurements from GPS and the conventional method was 0.705 cm. However, the rms error decreased to 0.5698 cm when applying the proposed method (see Fig.

33(a)). The improvement of the measurement accuracy can also be found in another comparison point (see Fig. 33(b)). The rms errors decreased from 2.413 cm to 1.1988 cm. Distinct disagreement of the conventional PSInSAR can be found in the duration from 2009-08-30 to 2009-10-30 due to serious effects of the stratified atmospheric phase delay at SAR acquisition time. Even though the atmosphere corrected PSInSAR has errors on the same dates, the errors were reduced and it could be the evidence for mitigating the APS. This comparison implies that the proposed method is quite efficient to extract the reliable volcanic deformation and mitigate the deterministic APS.

Indeed, above validation method might be insufficient for the evaluation of ground deformation at the summit of Shinmoedake volcano since the GPS stations are located below 400 m altitude. Another difference between the conventional PSInSAR and the atmosphere corrected PSInSAR is the estimated APS. The conventional PSInSAR assumed that the only temporally random phase is considered as the APS. In the suggested methods, APS can be explained as a sum of the stratified APS calculated from the WRF model and the turbulent APS estimated from high pass filtering (Fig. 34). For a comparison, the reference APS need to be set. MOD 05_L2 and MYD 05_L2 of MODIS data provide the integrated precipitable water vapor information with a spatial resolution of 1x1 km. It is possible to calculate the atmospheric phase delay from

MODIS data [Z. Li et al., 2005]. Fortunately, several MODIS data were available with little cloud and the acquisition time differences of only 10 min. The estimated APS from MODIS between 2008-05-27 and 2011-04-20 was chosen as the reference data for a comparison. In Fig 35, the estimated APS from the conventional PSInSAR shows disagreements from the APS from MODIS data, especially in Shinmoedake volcano. However, after processing of the atmosphere corrected PSInSAR, the estimated APS is quite similar even in Shinmoedake volcano. The correlation coefficient between the measured APS from MODIS and the estimated APS from the conventional PSInSAR is 0.3518. The scatter plot shows a strong linear relation between the measured APS from MODIS and the estimated APS from the atmosphere corrected PSInSAR and the correlation coefficient is 0.7505.

In addition, it is worth noting that spatial variation of the APS from the conventional PSInSAR is similar to that from the atmosphere corrected APS except on the mountain. High pass filtering is the APS estimation approach of the conventional PSInSAR to estimate the randomly generated phase in time. In fact, the turbulent APS is uncorrelated in time, and the turbulent APS can be mitigated in the conventional PSInSAR as well. However, if the stratified APS is severe and contaminate PSInSAR, the atmosphere corrected PSInSAR performs better than the conventional method.

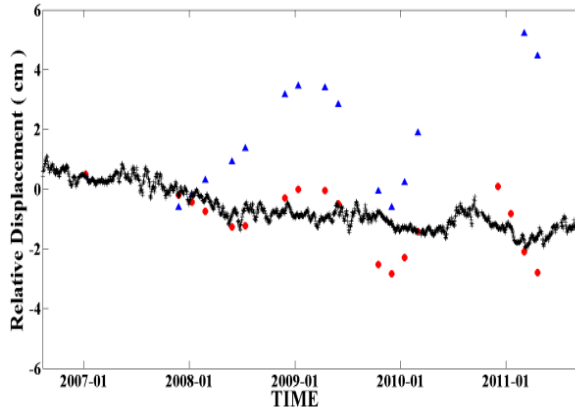


Fig. 32. Comparison between ground deformations. Black line is LOS displacement measured from GPS (West GPS-East GPS). Blue triangles are the ground deformation estimated from conventional SBAS and red circles are the estimated from atmosphere corrected SBAS.

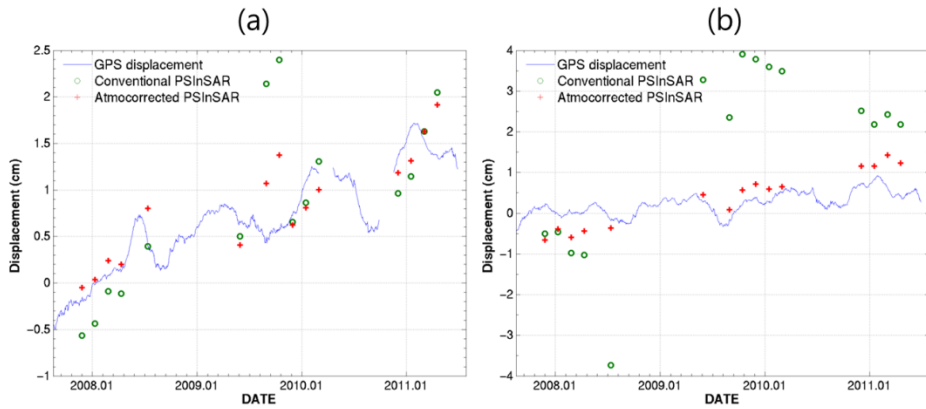


Fig. 33. The comparison of ground deformations measured at location of west GPS (a) and east GPS(b). Blue line is LOS displacement measured by GPS. Green circles are the ground deformation estimated from conventional PSInSAR and red crosses are that estimated from atmosphere corrected PSInSAR

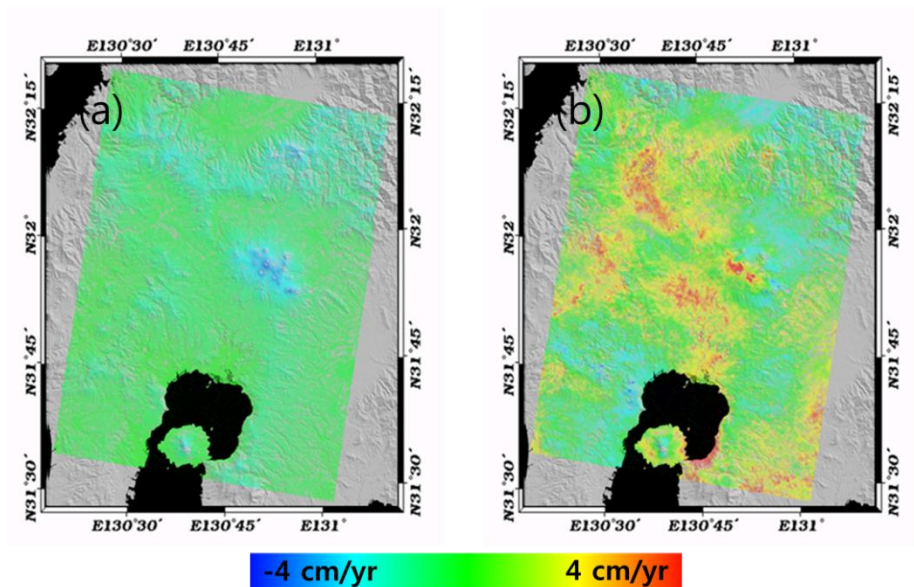


Fig. 34. (a) Stratified APS and (b) estimated turbulent APS from atmosphere corrected

PSInSAR in 2011-04-20

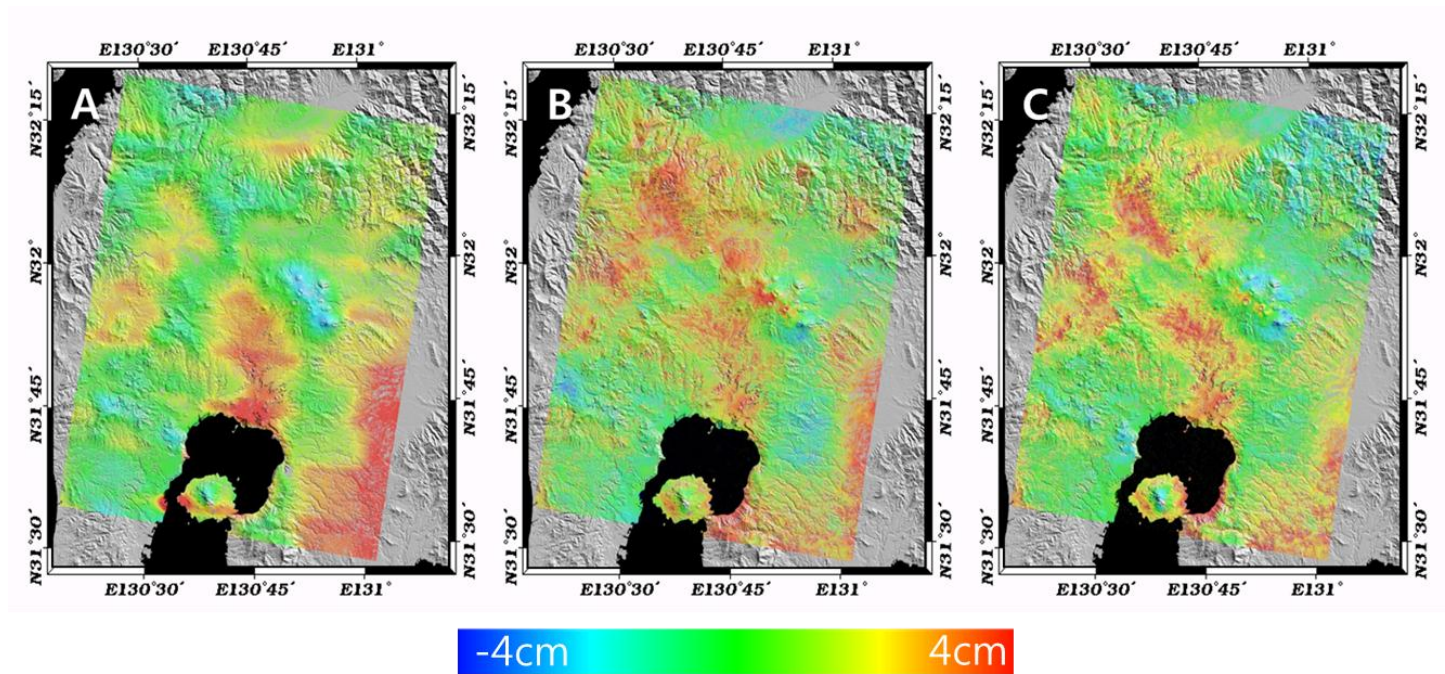


Fig. 35 The estimated APS between 2008-05-27 and 2011-04-20. A. the simulated APS from MODIS data. B. the estimated APS from conventional PSInSAR C. the estimated APS from atmosphere corrected PSInSAR

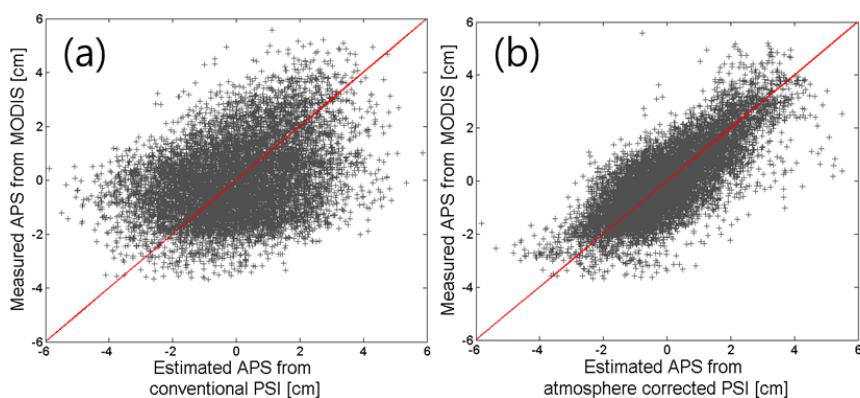


Fig. 36. (a) The scatter plot between the estimated APS from MODIS and conventional PSInSAR between 2008-05-27 and 2011-04-20 (b) The scatter plot between the estimated APS from MODIS and atmosphere corrected PSInSAR

6. Conclusion

The atmospheric phase delay is the one of the limitation of SAR Interferometry and differential interferometry. The efforts to mitigate the atmospheric phase delay have been yielded the great results [F. Beauducel et al, 2000; Z. Li et al., 2005; J. Foster et al., 2006; G. Nico et al., 2011; P. Berardino et al., 2002; A. Ferretti et al., 2000]. This research aims to minimize the atmospheric phase delay in differential interferograms for monitoring volcanic activities.

The first approach, i.e. atmospheric correction technique using MODIS data, gives quite good results and improves the accuracy of ground deformation. The biggest advantage in this technique is that it can be applied to numerous satellite dataset if MODIS data is available corresponding to SAR acquisition time. However, a lack of available dataset due to cloud coverage is a remaining limitation.

The second approach using a meso-scale weather forecasting model such as the WRF model has a potential to reduce the atmospheric errors. In spite of sufficient dataset, the accuracy of simulated meteorological data should be evaluated before correction, and the problem is inaccurate simulations of the turbulent atmospheric phase delay.

The time-series analysis also has errors in isolating APS from ground deformation. The APS estimation errors are mainly related to the stratified

APS. Since the WRF model has a potential to simulate the stratified APS, the stratified APS estimated from WRF model can mitigate the stratified APS in differential interferogram. In the case of the turbulent APS, low pass filtering in time is an effective method under the assumption that the turbulent APS is randomly generated. This assumption could be valid if the number of samples is sufficient enough to ensure the convergence of the random APS to zero.

In the case study of Shinmoedake volcano, the APS was successfully distinguished from the ground deformation. Since the relatively severe APS contaminate the ground deformation information, the residual APS still remained after processing the conventional methods. As a result, the ground deformation estimated from the conventional methods led to the misinterpretation of understanding the sequence of the volcanic activities. By applying the atmosphere corrected time series analysis, the estimated ground deformation yielded the reliable results associated with real physical volcanism. The ground deformation was validated with the GPS measurement. The estimated APS from the atmospheric phase delay reflected better distribution of APS, especially over the mountain and volcano than that from the conventional methods. Finally, the atmosphere corrected time-series analysis can be successful in measuring ground deformation caused by volcanic activities. Additionally, this method could be helpful to predict high resolution meteorological information.

However, the accuracy of the suggested method depends on the quality of the WRF model results. Therefore, the efforts to simulate the meteorological information which reflects realistic circumstances are required in the future study.

References

- A. Ferretti, C. Prati, F. Rocca, 2000, Nonlinear subsidence rate estimation using Permanent scatterers in differential SAR interferometry. *IEEE Trans. Geosci. Remote Sens.*, Vol. 38(5), pp. 2202-2212.
- A. Ferretti, C. Prati, F. Rocca, 2001, Permanent Scatters in SAR interferometry. *IEEE Trans. Geosci. Remote Sens.*, Vol. 39, pp.8-20.
- A. J. Hooper, 2006, Persistent scatterer radar interferometry for crustal deformation studies and modeling of volcanic deformation, California, USA: Stanford Univ. Press, Stanford
- A. Reigber, A. Moreira, 2000, First demonstration of airborne SAR tomography using multibaseline L-band data, *IEEE Trans. Geosci. Remote Sens.*, Vol. 38, Iss. 5, pp. 2142- 2152
- B. Rabus, M. Eineder, A. Roth, R. Bamler, , 2003, The shuttle radar topography mission—a new class of digital elevation models acquired by spaceborne radar, *ISPRS Journal of Photogrammetry and Remote Sensing*, Vol. 57, Iss. 4, pp. 241–262
- E. K. Smith, S. Weintraub, 1953, The constants in the equation for atmospheric refractive index at radio frequencies, *J. Res. Natl. Bur.Stand.*, Vol. 50, Iss.3, pp.9 - 41
- F. Beauducel, P. Briole, J.-L. Froger, 2000, Volcano-wide fringes in ERS synthetic aperture radar interferograms of Etna (1992-1998):

- Deformation or tropospheric effect?, J. Geophys. Res., Vol. 105(B7), pp. 16,391-16,402.
- F. Brenguier, N.M. Shapiro, M. Campillo, V. Ferirazzini, Z. Duputel, O. Coutant, A. Nercessian, 2008, Towards forecasting volcanic eruptions using seismic noise, Nature Geoscience, pp.126-130
- G. Nico, R. Tome, J.Catalao, P.M.A. Miranda, 2011, On the use of WRF model to mitigate tropospheric phase delay effects in SAR Interferogram, IEEE Trans. Geosci. Remote Sens., Vol. 49, no. 12, pp. 4970-4976
- G. Wadge, G.S.Mattioli, R.A. Herd, 2006, Ground deformation at Soufriere Hills Volcano, Montserrat during 1998-2000 measured by radar interferometry and GPS, Journal of volcanology and geothermal research, pp.157-173
- H.A. Zebker, P.A. Rosen, S. Hensley, 1997, Atmospheric effects in the interferometric synthetic aperture radar surface deformation and topographic maps, J. Geophys. Res., Vol. 102(B4), pp. 7547-7563
- J. Askne, H. Nordius, 1987, Estimation of tropospheric delay for microwaves from surface weather data, Radio Science, Vol. 22, no.3, pp.379-386
- J. Askne, J.O. Hagberg, 1993, Potential of interferometric SAR for classification of land surface, Geoscience and Remote Sensing Symposium, IGARSS '93. Better Understanding of Earth Environment, International Date of Conference: 18-21
- J. B. Johnson, R. C. Aster, P. R. Kyle, 2004, Volcanic eruptions observed with

- infrasound, *Geophys. Res. Lett.*, Vol. 31, pp. L14604, doi:10.1029/2004GL020020.
- J. B. Shepherd, R. A. Herd, P. Jackson, R. Watts, 1998, Ground deformation measurements at the Soufriere Hills Volcano, Montserrat: II: Rapid static GPS measurements June 1996-June 1997, *Geophys. Res. Lett.*, Vol. 25(18), pp.3413-3416, doi:10.1029/98GL01655
- J. Foster, B. Brooks, T. Cherubini, C. Shacat, S. Businger, C.L. Werner, 2006, Mitigating atmospheric noise for InSAR using a high resolution weather model, *Geophys. Res. Lett.*, Vol. 33, L16305
- J.G. Liu, A. Black, H. Lee, H. Hanaizumi, J. McM. Moore, 2001, Surface change detection in a desert area in Algeria using multi-temporal ERS SAR coherence images, *international Journal of Remote Sensing*, Vol. 22, Iss. 13
- J.G. Liu, P. Mason, F. Hilton, H. Lee, 2004, Detection of Rapid Erosion in SE Spain: A GIS approach based on ERS SAR coherence imagery, *Photogrammetric Engineering & Remote Sensing*, Vol. 70, No. 10, pp. 1179-1185.
- K. Mogi, 1958, Relation between the eruptions of various volcanoes and the deformation of ground surfaces around them, *Bulletin of the Earthquake Research Institute (University of Tokyo)*, Vol. 36, pp. 99–134
- K. Zhang, A. Hay-man Ng, X. Li, H.-C. Chang, L. Ge , C. Rizos, 2009, A new approach to improve the accuracy of baseline estimation for spaceborne

- radar interferometry, Geoscience and Remote Sensing Symposium, 2009
IEEE International, IGARSS 2009, Vol 5, pp.162-165
- M. Bevis, S. Businger, S. Chiswell, T. A. Herring, R.A. Anthes, C. Rocken,
R.H. Ware, 1994, GPS Meteorology: Mapping zenith wet delays onto
precipitable water. J. Appl. Meteor., Vol. 33, pp. 379-386.
- M. Crosetto, 2002, Calibration and validation of SAR interferometry for DEM
generation, ISPRS Journal of Photogrammetry and Remote Sensing, Vol.
57, Iss. 3, pp. 213–227
- M Simons, Y Fialko, L Rivera, 2002, Coseismic deformation from the 1999
M w 7.1 Hector mine, California, earthquake as inferred from InSAR and
GPS observations, Bulletin of the Seismological Society of America, vol.
92 no. 4, pp.1390-1402
- M. Tesauro, P. Berardino, R. Lanari, E. Sansosti, G. Fornaro, G. Franceschetti,
2000, Urban subsidence inside the city of Napoli (Italy) Observed by
satellite radar interferometry, Geophys. Res. Lett., Vol. 27(13), pp.1961-
1964
- P.A. Rosen, S. Hensley, H.A. Zebker, F.H. Webb, E.J. Fielding, 1996, Surface
deformation and coherence measurements of Kilauea Volcano, Hawaii,
from SIR-C radar interferometry, J. Geophys. Res., Vol. 101, No. E10, pp.
23109-23125
- P. Berardino, G. Fornaro, R. Lanari, E. Sansosti, 2002, A new algorithm for
surface deformation monitoring based on small baseline differential

- SAR interferograms, *IEEE Trans. Geosci. Remote Sens.*, Vol. 40(11), pp.2375-2383
- Q. Lin, J. F. Vesecky, H. A. Zebker, 1994, Comparison of elevation derived from INSAR data with DEM over large relief terrain, *International Journal of Remote Sensing*, Vol. 15, Iss. 9
- R. Hanssen, R. Bamler, 1999, *Radar Interferometry: Data interpretation and error analysis*, Kluwer Academic Publishers, Dordrecht, The Netherlands, pp. 308.
- R. M. Goldstein, C. L. Werner, 1998, Radar interferogram filtering for geophysical applications, *Geophys. Res. Lett.*, Vol. 25, no. 21, pp. 4035-4038
- S. Jonsson, H. Zebker, P. Cervelli, P. Segall, 1999, A shallow-dipping dike fed the 1995 flank eruption at Fernandina volcano, Galapagos, observed by satellite radar interferometry, *Geophys. Res. Lett.*, Vol. 26, no. 8, pp. 1077-1080
- S. Yun, P. Segall, H. Zebker, 2006, Constraints on magma chamber geometry at Sierra Negra Volcano, Galápagos Islands, based on InSAR observations, *Journal of Volcanology and Geothermal Research*, Vol. 150, Iss. 1–3, pp. 232–243
- W. C. Skamarock, J. B. Klemp, . J. Dudhia, D. O. Gil, D. M. Barker, M. G. Duda, X. Y. Huang, W. Wang, J. G. Powers, 2008, A description of the Advanced Research WRF Version 3, *Nat. Center Atmos. Res.*, Boulder,

- X. Ye, H. Kaufmann, X.F. Guo, 2004, Landslide monitoring in the three Gorges area using D-INSAR and corner reflectors, *Photogrammetric Engineering & Remote Sensing* Vol. 70, No. 10, pp. 1167-1172
- Y.J. Kaufman, C.C. Gao, 1992, Remote sensing of water vapour in the near IR from EOS/MODIS, *IEEE Trans. Geosci. Remote Sensing*, Vol. 30, pp.871-884
- Y. J. Kaufman, B.-C. Gao, 2003, Water vapor retrievals using Moderate Resolution Imaging Spectroradiometer (MODIS) near-infrared channels, *J. Geophys. Res.*, Vol. 108, no. D13, pp. 4389-4398
- Z. Li., M. Jan-Peter, C. Paul, 2005, Interferometric synthetic aperture radar (InSAR) atmospheric correction: GPS, Moderate resolution Imaging Spectroradiometer (MODIS), and InSAR intergration, *J. Geophys. Res.*, Vol. 110, pp. B03410.
- Z. Lu, D. Dzuurisin, J. Biggs, C.J. Wickes, S. McNutt, 2010, Ground surface deformation patterns, magma supply, and magma storage at Okmok volcano, Alaska, from InSAR analysis: 1. Intereruption deformation, 1997-2008, *J. Geophys. Res.*, Vol. 115, pp. B00B02

국문 요약

SAR 간섭 기법은 지표 변위 탐지에 적합한 기법으로 지진, 화산, 지반 침하 등 지표 변위가 관측 되는 현상에 대한 정보를 제공한다. 그러나 대기 위상 지연 효과로 인한 오차로 인하여 정밀한 분석이 어려울 수 있다. 화산에서는 다양한 대기 현상으로 인하여 지표 변위와 구별하기 힘든 오차를 발생시킨다. 본 연구에서는 SAR 간섭 기법을 화산에서 발생하는 정밀한 지표 변위를 탐지를 위하여 대기 위상 지연 효과를 보정할 수 있는 연구를 진행하였다.

다중 분광 자료를 이용하여 대기의 수증기량을 제공하는 MODIS 자료의 경우 대기의 수증기에 의하여 발생하는 마이크로 파의 지연 효과를 계산할 수 있다. 이와 같은 기법은 화산에 의하여 발생하는 지표 변위와 독립적으로 오차를 보정할 수 있다는 점과 관측 자료로서 비교적 정밀한 대기 위상 지연 효과를 계산 할 수 있다는 점에서 효율적인 대기 보정 기법으로 판단할 수 있다. 또한 현존하는 다양한 SAR 영상을 대상으로 대기 보정이 가능하다는 점에서 큰 장점이 있다. 그러나 MODIS 영상 내에 구름이 존재할 경우 수증기량 추출 알고리즘은 비교적 큰 오차를 야기하며, 이로 인하여 다수의 MODIS 자료를 이용하기 어려우며, 결과적으로 보정할 수 있는 자료의 개수는 화산 지표 변위를 연속적으로

이해하기 힘들기 때문에 한계가 있다고 할 수 있다. 또한 SAR 관측 시간과 MODIS 관측 시간의 차이는 추가적인 오차를 발생시킬 수 있다.

중규모 대기 예측 모델(WRF 모델)은 다양한 관측 자료로 분석된 자료를 기반으로 대기 모델을 사용하여 시공간에 따른 대기 현상을 계산한다. MODIS 영상과 달리 가용할 수 있는 자료의 양이 충분하다는 장점이 있으나, 모델에 대한 정밀도 검증이 추가적으로 필요하다. 본 연구에서는 라디오존데 자료를 사용하여 수증기의 연직 분포를 비교하였고 비교적 높은 상관성을 보이는 것을 확인하였다. WRF 모델을 사용하여 계산된 대기 위상 지연 효과는 차분 간섭도와 유사한 수증기의 분포를 보였으며, 특히 고도에 따라 발생하는 층상 대기 효과(Stratified APS) 효과를 감소시킬 수 있는 가능성을 보였다. 그러나 지역적으로 오차가 보였으며, 이는 불규칙적으로 발생하는 난류 대기 효과 (Turbulent APS)와 공간해상도의 차이로 나타났을 것이라고 예상된다.

PSInSAR 와 SBAS와 같은 시계열 분석 방법은 대기 오차가 시간적으로 상관성이 없다는 가정 하에 low pass filtering으로 지표 변위만을 계산한다. 그러나 WRF 모델로 계산된 대기 위상 지연 효과를 시계열 분석 방법으로 처리한 결과 잔여 대기 오차가 남아 있었으며, 이는 시간적으로 대기 위상 지연 효과가 발생할 수 있음을 지시한다. 화산 지표

변위 모델과 층리 대기 효과, 난류 대기 효과의 모델 결과에서는 불규칙적으로 발생하는 난류 대기 효과는 low-pass filtering으로 감소시킬 수 있으며, 층리 대기 효과의 경우 추가적인 보정 작업이 요구된다는 점을 나타냈다. 이는 앞서 제안된 WRF 모델로부터 가능하며, 이를 이용하여 PSInSAR와 SBAS에서 층리 대기 효과를 보정하는 기법을 제안하였다. 대기 위상 지연 효과와 지표 변위는 GPS와 MODIS로 계산된 대기 위상 지연 효과로 검증되었다. 본 연구에서 제안된 대기 보정된 시계열 분석 방법으로부터 추출된 대기 위상 지연 효과와 지표 변위는 기존의 PSInSAR와 SBAS 보다 관측자료와 잘 맞는다는 것을 확인할 수 있었다.

주요어 : SAR Interferometry, Atmospheric phase delay, Volcano, Ground deformation

학번 : 2011 - 20380